MOLECULAR DYNAMICS SIMULATIONS OF INTERFACIAL BEHAVIOR IN INDUSTRIAL COMPOSITE MATERIALS

NASIM SAMADPOUR

ÖZYEĞİN UNIVERSITY

AUGUST, 2025

MOLECULAR DYNAMICS SIMULATIONS OF INTERFACIAL BEHAVIOR IN INDUSTRIAL COMPOSITE MATERIALS

by
Nasim Samadpour

Thesis
Submitted in Partial Fulfillment of the
Requirements for the Degree of

Master of Science

in
Mechanical Engineering

Advisor: Assoc. Prof. İlknur Eruçar Fındıkçı
Co-advisor: Dr. Aydın Özcan

Graduate School of Science and Engineering
Özyeğin University
İstanbul

August, 2025

MOLECULAR DYNAMICS SIMULATIONS OF INTERFACIAL BEHAVIOR IN INDUSTRIAL COMPOSITE MATERIALS

Approved by:

Assoc. Prof. İlknur ERUÇAR FINDIKÇI
Advisor
Department of Natural and Mathematical Sciences
Özyeğin University

Asst. Prof. Hande ÖZTÜRK KAYMAKSÜT
Department of Mechanical Engineering
Özyeğin University

Asst. Prof. Esat Selim KOCAMAN
Department of Civil Engineering
Boğaziçi University

Approval Date: August 1, 2025

To my beloved family.

DECLARATION OF ORIGINALITY

I hereby declare that I am the sole author of this thesis and that this is the true copy of my thesis, including the final revisions, approved by my thesis committee. All data and information have been obtained, produced, and presented in accordance with the rules of research ethics and principles of academic honesty. As required by these rules, to the best of my knowledge I have acknowledged ideas, thoughts, and any copyrighted material in accordance with the standard referencing rules. I certify that any part of this thesis has not been submitted for a degree or diploma in another educational institution.

Nasim Samadpour

ABSTRACT

Composite materials are widely used in aerospace, automotive, and defense industries due to their excellent strength, high stiffness-to-weight ratio and corrosion resistance. Beyond these sectors, two other important areas for composites are the construction industry and natural gas purification. In construction, cementitious composites that incorporate recycled rubber have emerged as a promising approach to enhance concrete performance while mitigating the environmental impact of waste rubber, with nearly one billion tires discarded annually. In gas purification, polymer-based composite membranes are typically fabricated by embedding porous nanoparticles into a polymer matrix, thereby improving the separation performance and durability of the membranes. In both industries, the performance of composite materials is strongly influenced by the compatibility between their constituent components.

In rubber/concrete composites, the hydrophobic nature of rubber particles weakens their adhesion to the hydrophilic cement matrix, compromising the strength and durability of the composite. To overcome this limitation, improving the rubber-concrete interfacial bond is required to develop high-performance, sustainable construction materials. With this motivation, in the first part of the thesis, we build atomistic models of the rubber/Calcium Silicate Hydrate (CSH) interface and perform Molecular Dynamics (MD) simulations to investigate its structural properties using Radial Distribution Function (RDF) and by calculating the interfacial adhesion energy. We then evaluated several surface modification strategies to improve the bonding between rubber and cement. Specifically, we considered different polymers, including Polycarboxylate Ether (PCE), Carboxymethyl Cellulose (CMC) and Polyvinyl Alcohol (PVOH) between concrete and rubber. Among these, the rubber/concrete/PCE composite showed a 7.3% increase in interfacial adhesion energy of compared to the unmodified rubber-concrete composite.

In addition, when comparing the binding performance of CMC and PVOH, the rubber/-concrete/CMC composite exhibited a 17.08% higher interfacial adhesion energy than the rubber/concrete/PVOH system.

In the second part of this thesis, we investigated the carbon dioxide (CO_2) separation performance of composite materials used in the natural gas purification. We build atomistic models of Zeolitic Imidazolate Framework-8(ZIF-8)/Polymer of Intrinsic Microporosity-1 (PIM-1) interface. To assess gas separation behavior, we employed gas permeation models, including the classical Maxwell model and the modified Felske model, using adsorption and diffusion data obtained from Grand Canonical Monte Carlo (GCMC) and MD simulations. We studied both pristine PIM-1 and amine-functionalized PIM-1 (AF-PIM-1), each combined with either crystal ZIF-8 or ZIF-8 under pressure (aZIF-8@0.4GPa), to construct a variety of Mixed Matrix Membranes (MMMs). Our results showed that MMMs incorporating aZIF-8@0.4GPa with PIM-1 exhibit a modest (1.4%) increase in interfacial adhesion energy compared to those containing cryZIF-8 with PIM-1. Additionally, the modified Felske model provided more accurate predictions of MMM permeability, showing lower deviation from experimental results than the Maxwell model.

By analyzing different material classes including ZIFs, polymers and concrete, this thesis demonstrates that targeted surface or filler modifications can enhance interfacial bonding. The findings contribute to both the recycling of waste tires in the construction sector and the development of advanced membranes for gas separation.

Keywords: Composite materials, calcium silicate hydrate, interfacial adhesion energy, molecular dynamics simulations, ZIF-8 membrane

ÖZET

Kompozit malzemeler, hafiflikleri, yüksek mukavemet/ağırlık oranları ve korozyon dirençleri nedeniyle havacılık, otomotiv ve savunma sanayilerinde yaygın olarak kullanılmaktadır. Bu sektörlerin ötesinde, kompozitlerin kullanımına yönelik iki önemli alan ise inşaat sektörü ve doğal gaz ayrımıdır. İnşaat alanında, geri dönüştürülmüş kauçuk içeren çimento esaslı kompozitler, hem betonun performansını artırmak hem de her yıl yaklaşık bir milyar adet atık lastiğin çevresel etkisini azaltmak için umut verici bir yaklaşım olarak ortaya çıkmıştır. Gaz ayrımında ise, polimer esaslı kompozit membranlar genellikle gözenekli nanoparçacıkların bir polimer matrise gömülmesiyle üretilir, bu sayede membranların ayırma performansı ve dayanıklılığı artırılır. Her iki endüstride de, kompozit malzemelerin performansı, bileşenleri arasındaki uyumluluk tarafından büyük ölçüde etkilenmektedir.

Kauçuk/beton kompozitlerinde, kauçuk parçacıklarının hidrofobik doğası, onların hidrofilik çimento matrisiyle olan yapışmasını zayıflatmaktadır ve bu durum, kompozitin dayanımını olumsuz etkilemektedir. Bu sınırlamayı aşmak için, kauçuk ve beton arasındaki ara yüzey bağının iyileştirilmesi, yüksek performanslı ve sürdürülebilir yapı malzemelerinin geliştirilmesi açısından gereklidir. Bu motivasyonla, tezin ilk bölümünde kauçuk/kalsiyum silikat hidrat (CSH) ara yüzeyine ait atomistik modeller oluşturulmuştur ve moleküler dinamik (MD) simülasyonları ile bu ara yüzeyin yapısal özellikleri radyal dağılım fonksiyonu (RDF) ve ara yüzey yapışma enerjisi hesaplamaları yoluyla incelenmiştir. Ardından, kauçuk ve çimento arasındaki bağlanmayı iyileştirmek amacıyla çeşitli yüzey modifikasyon stratejileri değerlendirilmiştir. Bu kapsamda, beton ve kauçuk arasına poliakarboksilat eter (PCE), karboksimetil selüloz (CMC) ve polivinil alkol (PVOH) gibi farklı polimerler dahil edilmiştir. Bu çalışmalar sonucunda, kauçuk/beton/PCE kompozitinin, kauçuk-beton kompozitine kıyasla ara yüzey yapışma enerjisinde %7,3'lük bir artış

sağladığı gözlemlenmiştir. Ardından, CMC ve PVOH polimerlerinin bağlanma performansları karşılaştırılmıştır. Bu karşılaştırma sonucunda, kauçuk/beton/CMC kompoziti, kauçuk/beton/PVOH sistemine kıyasla %17,08 daha yüksek ara yüzey yapışma enerjisi sergilemiştir.

Tezin ikinci bölümünde, doğal gaz ayrımında kullanılan kompozit malzemelerin karbondioksit (CO_2) ayırma performansları incelenmiştir. Zeolitik imidazolat çerçevesi-8, ZIF-8 ve mikrogözenekliliğe sahip PIM-1 polimeri ara yüzeyine ait atomik modeller oluşturulmuştur. Gaz ayırma davranışını değerlendirmek için, Grand Kanonik Monte Carlo (GCMC) ve moleküler dinamik (MD) simülasyonlarından elde edilen adsorpsiyon ve difüzyon verileri kullanılarak, klasik Maxwell ve modifiye edilmiş Felske gaz geçirgenlik modelleri uygulanmıştır. Hem saf PIM-1 polimerini hem de amin fonksiyonel gruplarla modifiye edilmiş PIM-1 (AF-PIM-1) polimerini, kristal ZIF-8 (cryZIF-8) ve basınç altında sıkıştırılmış ZIF-8 (aZIF-8@0.4 GPa) ile birleştirerek farklı karışık yataklı membranlar (MMM) hazırlanmıştır. Sonuçlarımız, aZIF-8@0.4 GPa içeren MMM'lerin, cryZIF-8 içerenlere kıyasla PIM-1 ile birleşiminde ara yüzey yapışma enerjisinde %1,4 oranında hafif bir artış gösterdiğini ortaya koymuştur. Ayrıca, modifiye edilmiş Felske modeli, MMM gaz geçirgenliği için Maxwell modeline göre deneysel veriye daha yakın tahminler sunmuştur.

ZIF'ler, polimerler ve beton gibi farklı malzeme sınıflarının analiz edilmesiyle, bu tez, hedeflenmiş yüzey veya dolgu malzemesi modifikasyonlarının ara yüzey bağlanmasını artırabileceğini göstermektedir. Elde edilen bulgular, hem inşaat sektöründe atık lastiklerin geri dönüşümüne hem de gaz ayrımı için yeni membranların geliştirilmesine katkı sağlamaktadır.

Anahtar Kelimeler: Kompozit malzemeler, kalsiyum silikat hidrat (CSH), ara yüzey yapışma enerjisi, moleküler dinamik simülasyonlar, ZIF-8 membran, PIM-1.

ACKNOWLEDGEMENTS

This is the most meaningful part of my thesis for me, as it gives me the opportunity to thank all the people who have supported me throughout this wonderful journey. First of all, I am deeply grateful to my advisor, Assoc. Prof. İlknur Eruçar Fındıkçı, who not only guided me through my academic journey but also provided me with a new perspective on life. Through her endless support and guidance, I had the opportunity to develop myself.I am also sincerely grateful to my co-advisor, Dr. Aydın Özcan, whose insight and support have had a profound impact on both my academic and personal growth. I would like to express my gratitude to my committee members, Asst. Prof. Hande Öztürk and Asst. Prof. Esat Selim Kocaman, for their valuable insights, time, and constructive feedback.

I gratefully acknowledge the financial support of the Scientific and Technological Research Council of Türkiye (TÜBİTAK) for this master's research. My work began with Project No. 5220107 under the TEYDEB-1505 Program, in collaboration with Fibrobeton A. Ş., focusing on rubber–concrete composites. Working alongside experimental scientists provided me with invaluable insight into industrial practices. Upon completing this project, I began working on Project No. 222Z077 under TÜBİTAK 1001 Program, investigating atomistic simulations of ZIF-8/PIM-1 mixed matrix membranes. The numerical calculations reported in this thesis were partially performed using TRUBA resources at the TÜBİTAK ULAKBİM High Performance and Grid Computing Center, and partially carried out using the ÖzU HPC (Özyeğin University High Performance Computing Center) resources at Özyeğin University.

I am grateful to TÜBİTAK Marmara Research Center (TÜBİTAK-MAM) for providing such a supportive and stimulating environment. During my work on the TEYDEB 1505 Program project, I had the opportunity of conducting part of my research within the TÜBİTAK-MAM campus.

I deeply appreciate my beloved parents for their endless support and love. They have been a constant source of strength and inspiration throughout my life. I would not have been able to start this journey without their support. One of my deepest thanks goes to my dear Ali for his unwavering care, love, support, and understanding. He has always believed in me and reminded me never to give up on my dreams. I also feel lucky to have met my wonderful office mates, Parivash, Selen and Büşra. We shared countless hours of working, learning, and laughing together, and their friendship has made this journey all the more special. I want to express my heartfelt gratitude to my dear friend Zehra, whose constant support and encouragement have been invaluable to me, both personally and academically. I am also deeply thankful to my dear friends Su and Güneş for always being there for me, offering their kindness, encouragement, and understanding whenever I needed it most.

Permission to reproduce Figure 2.1 from Dongshuai Hou, "Background and Objectives," in Molecular Simulation on Cement-Based Materials, Springer Nature, 2020, is gratefully acknowledged.

TABLE OF CONTENTS

LIST OF TABLES

LIST OF FIGURES

LIST OF ACRONYMS AND ABBREVIATIONS

AF-PIM-1	Amine-Functionalized PIM-1
CMC	Carboxymethyl Cellulose
CSH	Calcium Silicate Hydrate
CH	Calcium Hydroxide
CCSU	Carbon Capture Storage and Utilization
CM	Crystal Maker
EPS	Expanded Polystyrene
EVA	Ethylene Vinyl Acetate
GCMC	Grand Canonical Monte Carlo
MMMs	Mixed Matrix Membranes
MOFs	Metal Organic Frameworks
MD	Molecular Dynamics
MS	Materials Studio
NVT	Canonical Ensemble
NPT	Isothermal–Isobaric Ensemble
PCE	Polycarboxylate Ether
PIMs	Polymers of Intrinsic Microporosity
PVOH	Polyvinyl Alcohol
PEG	Polyethylene Glycol
RDF	Radial Distribution Function

RH	Rubber Hydrocarbon
RC	Rubberized Concrete
SCMs	Supplementary Cementitious Materials
VMD	Visual Molecular Dynamics
WR	Waste Rubber
ZIFs	Zeolitic Imidazolate Frameworks
E	Total Energy
$\mathrm{k_B}$	Boltzmann constant
K	Kinetic Energy
H	Hamiltonian
LJ	Lennard–Jones
N	Particle Number
P	Pressure
U	Potential Energy
ϕ	Volume Fraction of Dispersed Phase
T	Temperature
T_m	Melting Temperature
T_d	Decomposition Temperature
V	Volume
Λ	Thermal de Broglie wavelength
ε	epsilon
σ	sigma

h	Planck's constant
ϕ	Volume fraction of the filler particles
P_r	Relative permeability
P	Effective permeability in the MMM
P_m	Permeability in the continuous polymer matrix
P_d	Permeability in the dispersed filler phase

1. INTRODUCTION

Composite materials are made by combining two or more substances with different physical or chemical properties [1]. This class of materials offer desirable properties including toughness, stiffness, light weight and corrosion resistance [2]. These exceptional characteristics are one of the reasons for their rapid growth in the fields of mechanical engineering and materials science [3, 4]. As a result, composite materials have become the preferred option in these fields and are quickly displacing traditional materials [5].

Despite the advantages of composite materials, a significant limitation has constrained their widespread adoption in industry. The performance of composites is highly sensitive to interfacial defects arising from incompatibility between their constituents. This incompatibility can create voids at the interface and lead to stress concentrations [1]. As a result, the strength of the interfacial bond strongly affects the mechanical, thermal, and electrical properties of the composite. Specifically, the interface governs mechanical load transfer across the material, affects thermal degradation and interfacial heat conduction, and influences particle dispersion and thus the composite's electrical conductivity [6]. Consequently, the characteristics of each constituent and their interactions with each other should be evaluated in detail before their selection for constructing composite materials. Both experimental and computational studies can guide the development of strategies to improve interfacial adhesion and, as a result, composite performance [6]. Modern composite engineering directly addresses interfacial bonding constraints in composites, with ongoing research focused on developing novel interfacial modification techniques [7]. In this thesis, we have focused on analyzing the interfacial compatibility in two critical application fields of composite materials: the construction and natural gas purification industries.

In construction industry, cementitious composites have emerged as transformative approaches, addressing the inherent limitations of conventional building materials. While steel, concrete, and cement have historically dominated the industry, their mechanical and environmental shortcomings, particularly cement's massive carbon footprint (approximately 1 ton carbon dioxide (CO_2) per ton produced) and concrete's poor tensile strength, have created an urgent need for advanced alternatives [8]. Calcium Silicate Hydrate (CSH) is the primary binding phase in concrete and the principal hydration product of cement [9]. Its porous, gel-like microstructure increases overall porosity and reduces the flexural and tensile strengths, and durability of concrete [10, 11].

In recent years, many efforts have aimed to overcome this intrinsic limitation of concrete. Incorporation of modifiers into concrete, including polymers like Polyethylene Glycol (PEG) [12] and Polyvinyl Alcohol (PVOH) [13], and carbon materials including graphene [14] and carbon nanotubes [15], causes improvements in concrete performance [16]. Notably, incorporating Waste Rubber (WR) in concrete has emerged as a practical, eco-friendly approach [17]. Compared with conventional concrete, rubberized concrete can exhibit excellent mechanical performance including high frost resistance, impact resistance, fatigue resistance, wear resistance, and shock absorption [17]. However, because rubber is hydrophobic and its elastic modulus differs from that of the hardened cement paste, microcracks and voids can form around the rubber particles, thereby reducing the mechanical strength of rubberized concrete [18]. To address this incompatibility, surface modification steps must be applied on rubber to increase its hydrophilicity and enhance the interfacial bond strength between rubber particles and concrete. In this regard, some researchers have done modification methods on rubber, including surface treatment with saturated NaOH [19], $KMnO_4$ and $NaHSO_3$ [20], acetic acid and calcium hydroxide [21], and silane coupling agent [22] solutions. According to their result, surface modification of rubber has strengthen the rubber/concrete interfacial bond.

Developing effective modification strategies for rubber requires a detailed understanding of rubber/concrete interfacial behaviour. In this thesis we have used Molecular Dynamics (MD) methods to understand the rubber/concrete interfacial zone from atomistic point of view. We started by constructing an atomistic model of concrete/rubber composite. The cementitious matrix contains abundant Ca^{2+} ions [9]. From an atomistic point of view, these ions determine the interfacial behaviour of concrete. Therefore, we can resolve the incompatibility between the two structures by introducing interfacial polymers between concrete and rubber that contain functional groups capable of interacting with these Ca^{2+} ions of concrete, such as carboxyl ($O-C=O$) and hydroxyl ($C-O$) groups. The first interfacial polymer we introduced is Polycarboxylate Ether (PCE). This polymer is commonly employed as a superplasticizer in concrete mixtures to reduce the amount of water required for blending [23]. In addition, it contains carboxyl functional groups, which are potential candidates for interacting with Ca^{2+} ions in the concrete matrix. For the next step, we aimed to identify a biodegradable alternative to PVOH, a non-biodegradable interfacial polymer that is commonly used in industry to bridge concrete and rubber [17]. We analyzed the interfacial behavior of Carboxymethyl Cellulose (CMC) [24], a biodegradable polymer and compared its compatibility performance with that of PVOH within the matrix. According to the literature, silane coupling agents improve the weak interface in rubber/concrete-based materials [25]. Therefore, to analyze their interaction mechanism, we developed atomistic models of carbon chains functionalized with SiO_2 groups and compared their performance with carbon chains functionalized with hydroxyl groups in acting as a bridge between concrete and rubber.

The applicability of composite materials extends beyond the construction industry to advanced gas separation technologies. In this domain, polymeric membranes are the primary technology used for gas separation [26, 27]. For example, commercial cellulose

acetate-based membranes are preferred for natural gas purification, offering CO_2/CH_4 selectivity of 10-20.3. Polymers of Intrinsic Microporosity (PIMs) are an important class of membranes for CO_2 separation, combining high permeability with moderate selectivity (9.08–31.6) through their microporous structures [28, 29]. Despite their advantages, polymeric membranes have a permeability-selectivity trade-off as empirically demonstrated by Robeson's upper bounds [30, 28]. In addition, physical aging and the limited stability of polymeric membranes in harsh environment conditions are critical issues that need to be addressed [31].

To address the limitations of polymeric membranes, nanoporous fillers are incorporated into the polymer matrix [32]. Metal Organic Frameworks (MOFs) are attractive candidates because they offer very high surface area and tunable pore structures. Among MOFs, Zeolitic Imidazolate Frameworks (ZIFs) constitute an important subclass [33, 34]. Their integration into polymer matrices creates Mixed Matrix Membranes (MMMs) that overcome the permeability-selectivity trade-off of polymeric membranes while preserving their processability. However, interfacial voids at the ZIF/polymer interface can affect the gas permeability of MMMs. One important issue in ZIF/polymer composites is polymer rigidification in the interfacial region, where the polymer is in contact with the ZIF structure. As a result, the gas permeability of the polymer near the interface is lower than that of the bulk polymer [35]. Interfacial compatibility is essential for producing homogeneous MMMs and minimizing permeability losses. Therefore, careful material selection is required to ensure the components are compatible with each other.

The second part of this thesis, focuses on constructing ZIF-8/PIM-1 MMMs. After constructing the model, we used MD simulations to systematically analyze the compatibility between constituent structures inside the composite. Specifically, we analyzed how the interfacial compatibility influences the gas permeability performance of the MMMs.

We began by modeling ZIF-8 as the filler phase and PIM-1 as the polymer matrix. To understand how interfacial compatibility between MMM layers influences overall gas permeability, we calculated the MMM permeability using two continuum models: Maxwell [36] and modified Felske [37] models. Unlike the Maxwell model, the modified Felske model accounts for the interfacial zone thickness in its calculations. Therefore, by comparing the gas permeability results from these two models with literature data, we aimed to understand the effect of the interfacial compatibility on the gas permeability of MMMs.

1.1 Thesis Overview

This study investigates two representative composite systems: cementitious composites used in the construction industry and ZIF-8-based composites for natural gas purification. Using equilibrium MD simulations, in both composite systems, we attempted to reveal the atomistic interactions in the interfacial zone and to understand how these interactions affect the overall compatibility of composites.

Chapter 2 of this thesis provided a literature review on cementitious composites and ZIF-8-based composites, separately. We focused on identifying key studies and methods that researchers had used to investigate these materials. In Chapter 3 we have described the computational methodology used in this study. We began by outlining the simulation tools and MD algorithms applied in our simulations. Then, we explained how we developed atomistic models for cementitious composites. We first modeled the CSH/rubber system, followed by various interface polymers, including PCE, PVOH, CMC, and functionalized carbon chains, which were inserted between CSH and rubber to reduce interfacial incompatibility. In the second part of Chapter 3, we described the modeling of ZIF-8-based composites. We created atomistic models of both crystalline and pressurized ZIF-8 frameworks. These structures were then embedded in either pure PIM-1 or amine-functionalized PIM-1 (AF-PIM-1) to form the final MMM systems. Chapter 4

presented the results of the MD simulations for both cementitious composites and ZIF-8-based MMMs. In both cases, we analyzed the interfacial interactions at the atomistic level and evaluated their effect on the overall performance of the composites. Finally, in Chapter 5, we evaluated the results of MD simulations and suggested possible ways to improve our approach to studying interfacial interactions in composite materials.

2. LITERATURE REVIEW

2.1 Experimental and Computational Studies on Cementitious Composites

Concrete is the material most used during the modern urbanization of human beings, which has profoundly affected the development and improvement of humanity in several eras. Meanwhile, it is the most widely used construction material for sidewalks, buildings, foundations, highways, roads, overpasses, parking garages, bricks, block walls, and foundations for gates, fences, and poles. Its range of applications exceeds that of all other building materials [38]. However, there are still some unresolved problems that require further investigation [39, 40, 41]. First, concrete has intrinsic defects: (1) its tensile and flexural strength is significantly lower than its compressive strength. As a result, the tensile and flexural strength of concrete is only about 10% and 15% of its compressive strength, respectively [42]. (2) The hydration process of concrete inevitably leads to chemical shrinkage [43]. Furthermore, concrete can exhibit autogenous shrinkage, drying shrinkage, and creep under certain conditions. Secondly, the production of Portland cement, the main concrete component, is very energy intensive. For every ton of Portland cement produced, around 0.85 tons of CO_2 are emitted [44]. Therefore, the growing demand for concrete poses a significant threat to the natural environment. Third, concrete is susceptible to attack by aggressive ions present in the environment [45, 46]. In marine or brine environments, aggressive ion attack can lead to expansion, cracking, or even loss of the cohesive strength of concrete [47]. The early failure of concrete structures increases the need for their repair or replacement, further increasing their environmental harm. Therefore, various approaches have been taken in the concrete production process to introduce new method to reduce its environmental footprint [48, 49]. For example, rebar or steel fibers can be incorporated into concrete to increase its tensile and flexural strength. Expansion agents are used to compensate for shrinkage, mineral admixtures or

polymers are incorporated to improve durability, and Portland cement can be completely replaced with Supplementary Cementitious Materials (SCMs) to promote sustainability in the construction industry. As a result, traditional "Portland cement concrete" is now more commonly referred to as "cementitious materials". However, these measures only improve the specific properties or aspects of cementitious materials. Research and modification efforts are moving towards the nano scale approaches with the growing understanding of their specific behavior [9].

Nanotechnology is a field that considers materials at the atomic scale and has effects and applications at the real-world level. The unique physical and chemical properties of nanomaterials can be used in ways that benefit the global community [50]. Since nanotechnology was first introduced by Nobel laureate Richard P. Feynman in his well-known 1959 lecture "There is Plenty of Room at the Bottom", significant advances in physics, chemistry, and biology have shown the feasibility of his vision: Manipulating matter at the nanoscale, down to molecules and atoms [9, 51, 52]. Similarly, studying and modifying cement-based materials at the nanoscale is essential to improve their performance.

Cement paste is a porous material consisting of different phases. When cement powder is mixed with water, a chemical reaction called hydration takes place. This reaction produces several important compounds found in concrete: CSH, Calcium Hydroxide (CH), ettringite and monosulfoaluminates. CSH makes up about 50–70% of the final product and is the main factor in the strength of cement-based materials [9, 53, 54]. For this reason, studying and improving the structure of CSH gel is very important to make cement materials stronger. However, as shown in Figure 2.1, due to the hierarchical nature of concrete, its structure spans multiple length scales. At the nanoscale ($< 10^{-9}\,\mathrm{m}$), CSH adopts a basic framework in which Ca, Si, and OH^- groups are distributed. Due to the complex composition, structure and physical behavior of CSH gel, its basic building blocks are still not fully understood [9, 55].

Figure 2.1: *Hierarchical structure of concrete. Reprinted from [9] with permission of Springer Nature.*

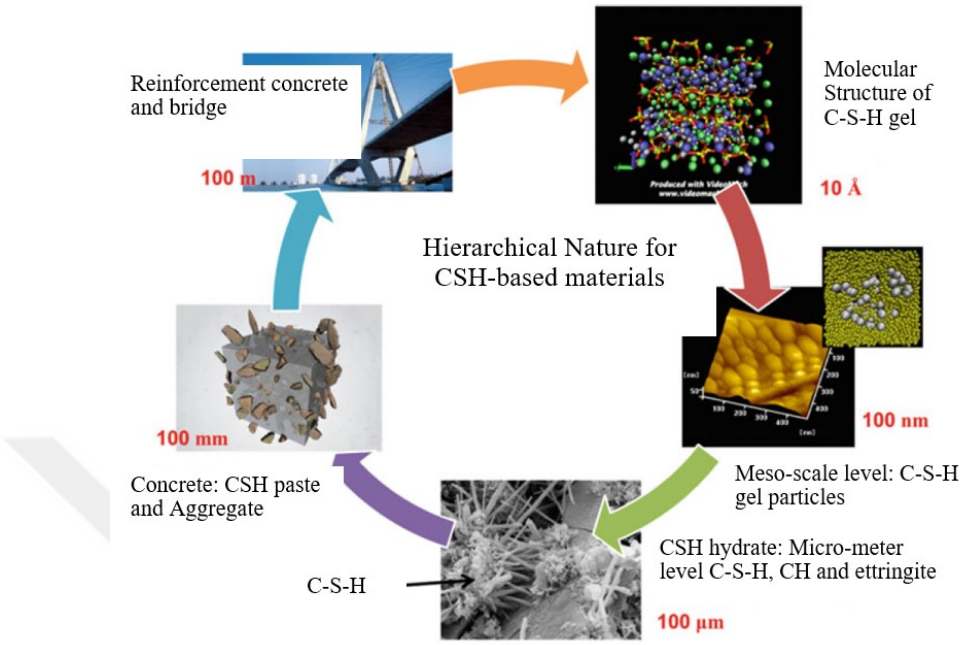

Because the CSH gel functions as the "DNA" of concrete, a detailed understanding of its structure is crucial. For example, the mechanical properties of CSH gel are fundamental because the behavior at the nano- and microscale provides the structure cohesion that supports the material's performance at the macroscale [9].

The other critical aspect related to cementitious composites is their sustainability and use of the waste aggregates emerge as a critical approach. The management of waste tires is a significant ecological challenge due to the non-biodegradable nature and excessive environmental residence time of WR [56, 57, 58, 59, 60]. According to the 2018 World Bank report What a Waste 2.0: A Global Snapshot of Solid Waste Management to 2050 [61], global waste generation is expected to increase significantly [62]. By 2050, the total volume of waste is expected to increase by 70%, from 2.01 billion tons in 2016 to 3.4 billion tons. With growing concerns over solid waste, recycling end-of-life tires remains a significant challenge for researchers and environmental organizations [62]. Another

study reports that global natural rubber production has increased by 4.1% over time and by 13.6% annually to 941,000 tons, while annual consumption has increased only slightly by 0.3% to 1.21 million tons [63, 64]. This imbalance between production and consumption rates reflects a key environmental issue related to waste tires. It underlines the urgent need for practical solutions to manage residual scrap rubber and avoid potential ecological risks. Therefore, reusing waste tires and developing effective methods to reduce their environmental impact remains a significant ecological challenge today.

Conventional methods for managing end-of-life tires, such as landfilling, retreading, and incineration [65] are inadequate for solving environmental problems and also cause additional environmental damage. Landfilling, for example, takes up large land areas and releases pollutants in ecologically sensitive regions [58]. When used tires are incinerated in an open environment, toxic gasses and volatile compounds are released, including arsenic, mercury, hydrocarbons, organic substances, cadmium, and chromium. These emissions pose a serious fire hazard and a human health risk [66, 67]. Although reusing tires appears cost-efficient in the short term, it delays the disposal problems. Ultimately, tires end their life and accumulate in the environment [60]. One of the most effective modern approaches to reduce the impact of waste rubber is to recycle it into crumb rubber. This crumb rubber is used as reinforcement in commonly used construction materials such as concrete [68, 69, 70, 71, 72]. Thus, recycling WR into crumb rubber as concrete reinforcements not only offers a sustainable solution to waste tire management but also contributes to the realization of greener building materials. In recent years, there has been a growing interest in the use of rubber in concrete, leading to the development of what is now known as Rubberized Concrete (RC). Since the 1990s, the method of replacing aggregate in concrete with WR has become increasingly popular [73, 74, 75, 76]. This approach not only recycles WR, thereby safeguarding the environment, but it also enhances several properties of concrete, such as toughness [77], dumping capacity [78]

and freeze-thaw resistance [75], among others [76]. Despite the benefits of rubber concrete, integrating rubber into the cement matrix poses significant challenges, primarily due to the interfacial properties of rubber. The poor bonding of rubber particles with cement paste significantly affects the mechanical properties and durability of the composite. To address this issue, improving the bonding performance of rubber particles has proven beneficial. This improvement leads to better mechanical properties. It also increases the durability of the rubber-concrete composite [79]. Therefore, although RC has many benefits, further improvements in bonding are essential for its success as a sustainable building material.

To overcome the challenges associated with RC, researchers have implemented various experimental and computational studies. For example, Li et al. [80] conducted a study using a two-stage surface modification process on rubber. They applied a silane coupling agent and carboxylated styrene–butadiene rubber latex to develop chemical bonds between rubber and cement paste. As a result, the concrete containing treated rubber showed a significant increase in both compressive and flexural strength compared to concrete containing untreated rubber. Chou et al. [70] investigated the effects of partial oxidation on RC to address compatibility issues between rubber and concrete. They discovered that partial oxidation leads to the formation of hydrophilic functional groups (S=O and S-O) on the surface of crumb rubber. This enhances cement hydration and significantly improves the mechanical properties of the rubberized mortar. Rivas et al. [81] investigated the surface treatment of recycled rubber using three different solvents: ethanol, acetone, and methanol. They evaluated the compressive strength, performed slump tests, and conducted Fourier Transform Infrared Spectroscopy on the concrete samples. Their findings indicated that the rubber treated with solution of acetone demonstrated the most significant potential to enhance the mechanical strength of the RC. Zhang et al. [82] applied a pretreatment to rubber particles using acrylic acid and PEG. Their experimental

analysis showed that this treatment led to a significant increase in the contact angle between the rubber particle surface and water. Additionally, they observed an increase in both the compressive and flexural strengths of the modified rubber concrete.

Meanwhile, only limited number of computational research has thoroughly investigated the compatibility challenges of using rubber in cementitious matrices. To improve the compatibility between rubber particles and cement, Young et al. [63] integrated PVOH fibers and a silane coupling agent, KH570, thereby enhancing both compatibility and structural integrity. This combination significantly improved the bonding at the interface, leading to a denser, more cohesive material. MD simulations further demonstrated that KH570 induced a structural transition at the rubber interface, promoting better interaction with cement components. In another study, Yong et al. [83] focused on Expanded Polystyrene (EPS)-concrete, using Ethylene Vinyl Acetate (EVA) as an interface modifier. Their research included a comparative analysis of interaction energy, Radial Distribution Function (RDF), and the mechanical properties of the EPS-concrete structure, both before and after the application of EVA. Notably, the addition of EVA improved the rigidity and bonding quality of the EPS-concrete structure. Lijuan et al. [84] performed an MD simulation, to explore the interactions between epoxy resin and rubber at along a cementitious interface. Their findings indicated that adding epoxy resin not only improved the interaction energy at the interface but also increased the number of hydrogen bonds. Further analysis of mechanical properties showed that the elastic modulus at the interface was enhanced, significantly improving the interface properties with the inclusion of epoxy resin. Overall, previous studies have developed effective techniques to improve both the mechanical and environmental properties of RC, setting the stage for further advancements in sustainable building practices. The first part of thesis presents atomistic simulations to evaluate how several candidate polymers can improve the interfacial adhesion between rubber and CSH.

2.2 Experimental and Computational Studies on Polymer/ZIF-8 Composites

Carbon Capture Storage and Utilization (CCSU) technologies play a crucial role in addressing climate change and fulfilling objectives related to carbon neutrality [85, 86, 87]. Among various greenhouse gases CO_2 is pivotal in driving environmental challenges [88, 89]. CO_2 accounts for approximately 76% of total greenhouse gas emissions, followed by methane (CH_4) at 16% and nitrogen oxides (NO_X) at 6%. Due to this distribution, greenhouse gas emissions are commonly expressed in terms of CO_2 equivalents [90]. Over the past century, atmospheric CO_2 concentrations have nearly doubled, primarily due to escalating fossil fuel usage and increasing energy demands [88]. The remaining carbon budget required to limit global warming to 1.5°C decreased by 10% to 66.7% during 2023, indicating that allowable emissions may be exhausted within approximately 0.5 to 6 years (with a 67% probability) [91]. The unregulated release of CO_2 into the atmosphere has had severe and lasting impacts on the environment. These impacts include environmental, ecological, physical, and economic domains and public health. They include intensified weather patterns such as heatwaves, rising sea levels, which lead to irregular floods and droughts, ultimately disrupting agricultural cycles [92, 93]. About 30% of global CO_2 emissions come from industrial activities: 24.2% from the energy consumed by the industrial sector and 5.2% from direct process emissions, mainly in chemical and cement production [94, 95].

Four primary approaches are commonly considered to capture CO_2 emissions according to their relative sources: pre-combustion capture, post-combustion capture, chemical looping combustion, and oxy-combustion. Among these, oxy-combustion and pre-combustion capture are incompatible with existing power plants and are, therefore, more applicable to newly built facilities [96, 97]. Post-combustion technologies involve capturing CO_2 from the flue gas emitted by power plants that burn fossil fuels [96, 98]. This

approach is preferred, as it can be upgraded to existing power plants that use air for fuel combustion. Several post-combustion CO_2 capture technologies are available, including membrane separation, absorption, adsorption, and cryogenic separation [96, 99]. Absorption is currently the most widely employed and effective method for removing CO_2 from synthesis and natural gas streams [96, 97]. However, these technologies are associated with significant drawbacks, primarily high costs and substantial energy consumption. Adsorption methods also face challenges, particularly due to costly regeneration processes. In cryogenic separation, acidic gases are frozen to isolate CO_2 in liquid form; however, the major limitation of this technique is the high power demand required to operate the refrigeration unit. Membrane separation, on the other hand, is an emerging and rapidly advancing technology for CO_2 capture. It offers several advantages over traditional methods, including operational simplicity, flexibility, adaptability, environmental compatibility, low energy requirements, continuous operation, reduced maintenance costs, and a smaller physical footprint [96, 100].

Over the past decades, a wide range of membrane materials have been employed for CO_2 capture, including metal oxides, basic salts, layered double hydroxides, ionic liquids, and porous materials such as activated carbon, carbon fibers, zeolites, and MOFs [33]. Compared to other materials, MOFs are considered among the most promising membrane candidates due to their exceptionally large surface area. However, moving from laboratory-scale innovations to industrial-scale applications involves considerable obstacles [101, 102]. Few suitable MOFs for real-world applications have been successfully produced on a large scale. There is an urgent need to develop strategies that accelerate the transition from lab-scale materials to industrial-scale products. A thorough understanding and analysis of existing barriers is required to achieve this transition. For example, most MOF synthesis methods are only feasible under laboratory conditions due to accurate reaction requirements such as high temperatures, long reaction times, humidity

control, and hazardous chemicals [101]. Another challenge is the stability of MOFs under practical conditions; most MOFs featuring metal-carboxylate linkages exhibit instability in water or humid environments [103, 104]. In addition, post-synthesis processes such as drying and shaping MOF materials can result in structural degradation or alterations in their porous frameworks.

ZIFs are exceptional porous materials and an essential subclass of MOFs with well-defined pore networks, high stability, and outstanding gas-separation performance [32]. For example, the gas selectivity of ZIF-8 for H_2/CO_2 and H_2/CH_4 separations ranges from 4.3–69.1 and 3.96–39.1, respectively, depending on the fabrication route and testing conditions [105].

Amorphous ZIF membranes constitute a new class of materials that integrate the structural and functional attributes of crystalline ZIFs with the intrinsic advantages of glassy materials [31]. In recent years, research attention has increasingly focused on the synthesis of glassy (amorphous) ZIFs through the pressing and melt-quenching of crystalline ZIFs [106, 107]. During the melting process, the ZIF glass loses its long-range ordered structure but retains short-range units, eliminating grain boundaries. Consequently, glassy ZIF membranes offer easier preparation and processing advantages compared to other ZIF membranes [106]. When the melting temperature of a ZIF reaches its upper limit, its framework remains thermally stable without decomposition, enabling the formation of a ZIF glass through subsequent melting and quenching. Thus, melting temperature (Tm) of ZIFs must be lower than their decomposition temperature (Td) [106, 108]. Specifically, ZIF glasses exhibit unique transport properties, such as selective permeability, which makes them particularly attractive for gas separation applications [109]. For example, Mahdavi et al. [110] fabricated a self-supporting glassy ZIF-62 membrane and systematically evaluated its gas separation performance. The optimized membrane achieved selectivities of 223.5 (H_2/CH_4), 64.1 (CO_2/CH_4) and 3.49 (H_2/CO_2), alongside

high permeabilities of 509 Barrer for H_2, 146 Barrer for CO_2 and 2.28 Barrer for CH_4. These values surpass those of conventional crystalline ZIF-62 membranes and place the material on the 2015 Robeson upper bound [111]. In another study, Ma et al. [112] examined the amorphization of ZIF-8 by applying a mechanical pressure of 0.75 GPa. They reported ideal selectivities of 14.79 for (H_2/CH_4) and 16.23 for (CO_2/CH_4). Although glassy ZIF membranes offer significant advantages for gas separation process, they can retain only a portion of their inherent porosity. This porosity can be optimized through layering with other materials such as porous polymers to develop MMMs [106].

Amorphous ZIF-based MMMs integrate the beneficial attributes of ZIFs with polymer matrices, producing hybrid membranes with enhanced gas separation performance [31, 113, 114]. These composites exhibit improved properties compared to pure amorphous ZIFs and pure polymeric membranes [115]. For example, Feng et al. [116] created an amorphous ZIF-62/PIM-1 membrane by giving ZIF-62/PIM-1 precursor films an optimized in-situ thermal treatment. The resultant amorphous ZIF-62/PIM-30% membrane had a CO_2/CH_4 selectivity of 67 and a CO_2 permeability of 5914 Barrer, surpassing the 2019 Robeson upper bond [28]. Zhang et al. [117] proposed a novel strategy for fabricating ZIF-based MMMs by dispersing a ZIF-8 gel within a PIM-1 polymer matrix. The resultant membranes exceeded the 2008 upper bound [30] with a 78.9% increase in H_2 permeability (beyond 6800 Barrer) and a 38.0% increase in H_2/CH_4 selectivity at a ZIF-8 gel loading of 31.0 wt%. Kertik et al. [118] investigated polyimide-based MMMs incorporating amorphous ZIF-8. The membrane with 30 wt.% amorphized ZIF-8 showed a CO_2 permeability of 47.9±0.48 Barrer under 10 bar, 35°C, and a 50/50 CO_2/CH_4 gas mixture. In comparison, an MMM with 30 wt.% crystalline ZIF-8 achieved only 4.5±0.6 Barrer under the same conditions.

In the second part of this thesis, we used MD simulations to study the interfacial interactions in ZIF-8/PIM-1-based MMMs.

3. COMPUTATIONAL METHODOLOGY

3.1 Simulation Tools

The main computational environment used in this study was the Large-scale Atomic/Molecular Massively Parallel Simulator (LAMMPS) [119] package. The msi2lmp [120] package was used to parameterize the structures with associated force fields. In addition, the initial atomic configurations were constructed using Materials Studio (MS) [121] and Crystal Maker (CM) [122] software. Post-processing analysis, including RDF and density analysis, and adhesion energy calculation, were performed in Python [123]. Visual Molecular Dynamics (VMD) [124], OVITO [125], and CM software were used for visualization.

3.2 Details of Molecular Dynamics (MD) Simulations

The MD simulations were performed using the LAMMPS [119] package. For each system, the initial cartesian coordinates were supplied in a structure file, like PDB, CIF, or the LAMMPS data format, chosen according to the specific simulation workflow. The MD simulation begins by importing the initial cartesian coordinates (x,y,z) of atoms and assigning random initial velocities to each of them. LAMMPS then uses the user-specified seed number supplied in the corresponding command to initialize its internal pseudorandom-number generator. The seed number controls the generation of Gaussian random numbers used to assign particle velocities from the Maxwell–Boltzmann distribution (Eq. (3.1)) [126] at the target temperature. This ensures both correct sampling of the canonical ensemble and exact reproducibility of every trajectory.

$$f(v) \;=\; \left(\frac{m}{2\pi k_B T}\right)^{\frac{3}{2}} 4\pi v^2 \exp\!\left(-\tfrac{mv^2}{2k_B T}\right) \tag{3.1}$$

For the Maxwell–Boltzmann speed distribution, the characteristic scale parameter a,which sets the width of the distribution, is defined as the square root of the ratio between

the thermal energy per degree of freedom and the particle mass [127]:

$$a = \sqrt{\frac{k_{\mathrm{B}}\, T}{m}} \tag{3.2}$$

where the ($\mathbf{k}_{\mathrm{B}}$) is Boltzmann constant, T is the absolute temperature, and m is the mass of an individual particle.

Computer simulations in condensed physics are mainly based on analyzing the characteristics and dynamics of materials from an atomistic point of view [128, 129, 130, 131]. This method is theoretically grounded in statistical thermodynamics. Classical MD is the most straightforward approach conceptually [132, 133, 134]. Through MD simulation, we simply solve the Newton's equation of motion among interacting particles. By iterating these calculations at each time step, we obtain a time-resolved trajectory that captures the complete dynamical evolution of the system. Finally, the time averages of the desired observations are calculated along this trajectory [131]. Newton's equation of motion conserves the total energy (E), and the other thermodynamic variables, such as temperature (T) and pressure (P), can only be inferred indirectly and have fluctuations over the simulation time [131]. In this thesis, we mainly conducted the MD simulations under two ensembles, canonical ensemble (NVT) and isothermal–isobaric ensemble (NPT). In the NVT ensemble, simulations are carried out at fixed particle number (N), volume (V), and T, so the P is free to fluctuate. By contrast, the NPT ensemble constrains N, P, and T, allowing the system volume to adjust dynamically to sustain the prescribed pressure.

Over the years, several alternative algorithms have been implemented in MD, most notably the widely recognized velocity-Verlet [135] integrator [136, 137, 138, 139]. Because of its remarkable stability and ease of use, this second-order integrator is frequently used in MD simulations [139]. Using the Verlet integration algorithm, we model a system of N particles whose cartesian positions are gathered as $\vec{X} = \{\vec{r}_i\}$, i = 1,2,...,N, in a d-dimensional space. Newton's second law is numerically integrated for every particle in

MD simulations [128].

$$m_i \ddot{\vec{r}}_i \;=\; -\frac{\partial U_{\text{pot}}}{\partial \vec{r}_i} \;=\; \vec{f}_i \tag{3.3}$$

where m_i is the mass of particle i and $\vec{f}_i$ is the force acting on it, assumed to arise exclusively from interactions with the other particles in the system. Hence the potential energy $U_{\text{pot}}(\vec{X}) = U_{\text{pot}}(\vec{r}_1, \ldots, \vec{r}_N)$ is expressed as follows:

$$U_{\text{pot}} = \sum_{i=1}^{N-1} \sum_{j>i}^{N} U(\vec{r}_{ij}), \qquad \vec{r}_{ij} = \vec{r}_i - \vec{r}_j \tag{3.4}$$

and the force acting on particles:

$$\vec{f}_i \;=\; -\sum_{j\neq i} \frac{\partial U(r_{ij})}{\partial \vec{r}_i} \;=\; \sum_{j\neq i} \vec{f}_{ij} \tag{3.5}$$

The total energy:

$$E \;=\; E_{\text{kin}} + U_{\text{pot}} \;=\; \sum_{i=1}^{N} \frac{1}{2}\, m_i \dot{\vec{r}}_i^{\,2} \;+\; U_{\text{pot}} \tag{3.6}$$

Since the total energy does not change with time we have:

$$\frac{\mathrm{d}E}{\mathrm{d}t} \;=\; \sum_{i=1}^{N} m_i \dot{\vec{r}}_i \ddot{\vec{r}}_i \;-\; \sum_{i=1}^{N} \dot{\vec{r}}_i \cdot \vec{f}_i \;=\; 0 \tag{3.7}$$

As it can be seen from the Eq. (3.7) the Newton's equations of motions are integrated numerically in MD [128]. To drive the Verlet algorithm [136], we expand $\vec{r}_i(t)$ forward and backward in time:

$$\vec{r}_i(t+\delta t) = \vec{r}_i(t) + \delta t\, \vec{v}_i(t) + \frac{1}{2m_i}(\delta t)^2 \vec{f}_i(t) + \frac{1}{6}(\delta t)^3 \vec{b}_i(t) \tag{3.8}$$

$$\vec{r}_i(t-\delta t) = \vec{r}_i(t) - \delta t\, \vec{v}_i(t) + \frac{1}{2m_i}(\delta t)^2 \vec{f}_i(t) - \frac{1}{6}(\delta t)^3 \vec{b}_i(t) \tag{3.9}$$

Here, $v_i(t)$ denotes the velocity of particle i at time t, and $b_i(t)$ is the corresponding vector that appears in the third–order term of the Taylor expansion. When the two expansions are added, the odd–order terms cancel out [128]. So we have:

$$\vec{r}_i(t+\delta t) \;=\; 2\,\vec{r}_i(t) \;-\; \vec{r}_i(t-\delta t) \;+\; \frac{1}{m_i}(\delta t)^2 \vec{f}_i(t) \tag{3.10}$$

Subtracting the two expansions yields the velocity:

$$\vec{v}_i(t) \;=\; \frac{1}{2\,\delta t}\big[\,\vec{r}_i(t+\delta t) - \vec{r}_i(t-\delta t)\big] \tag{3.11}$$

The Verlet algorithm [128, 134, 136, 140, 141] is explicitly time–reversible: interchanging $\vec{r}_i(t+\delta t)$ and $\vec{r}_i(t-\delta t)$ produces the propagator for backward time evolution and changes the sign of the velocities [128].

A characteristic of the standard Verlet scheme is that the velocity update lags by one time step: the velocities at time t can only be evaluated once the positions at $t+\delta t$ are known (Eq. (3.11)). In the velocity Verlet algorithm [142], position and velocity updates are performed synchronously, [128] as follows:

$$\vec{r}_i(t+\delta t) \;=\; \vec{r}_i(t) + \delta t\,\vec{v}_i(t) + \frac{1}{2m_i}(\delta t)^2\,\vec{f}_i(t) \tag{3.12}$$

To sum up, MD simulations update atomic positions and velocities at each timestep using numerical integration schemes, most commonly variants of the Verlet family; in this work, we employ the velocity-Verlet integrator.

The Hamiltonian (H) of a system containing N molecules can be written as the sum of a kinetic energy (K) term and a potential energy (U) term, each expressed in terms of the generalized coordinates $\mathbf{q}_i$ and momenta $\mathbf{p}_i$ of molecule i [128]. Using compact notation, it takes the form:

$$H(\mathbf{p},\mathbf{q}) \;=\; K(\mathbf{p}) + U(\mathbf{q}) \;=\; \sum_{i=1}^{N} \frac{\mathbf{p}_i^2}{2m_i} \;+\; U\big(\mathbf{q}_1,\ldots,\mathbf{q}_N\big) \tag{3.13}$$

where $K(\mathbf{p})$ denotes the total kinetic energy and $U(\mathbf{q})$ represents the potential energy that captures all intermolecular interactions. The Hamiltonian of a system is usually equal the total internal energy E of the system [128]. The kinetic-energy contribution can be expressed explicitly in terms of the conjugate momenta as follows:

$$\mathcal{K} \;=\; \sum_{i=1}^{N}\sum_{\alpha} \frac{p_{i\alpha}^2}{2\,m_i} \tag{3.14}$$

where m_i is the mass of molecule i, and the index α runs over the Cartesian components (x, y, z) of the momentum $p_{i\alpha}$ of atom i. In classical molecular simulations, the total potential energy U is decomposed into intramolecular (bonded) contributions, namely bond-stretching, angle-bending, dihedral torsions, and improper torsions, and intermolecular (non-bonded) contributions, represented by the Lennard–Jones (LJ) and Coulombic potentials [128]:

$$U \;=\; U_{\text{bond}} + U_{\text{angle}} + U_{\text{dihedral}} + U_{\text{improper}} \;+\; U_{\text{LJ}} + U_{\text{Coulomb}} \tag{3.15}$$

In this thesis we used the 12–6 LJ potential to model van der Waals (dispersion–repulsion) interactions:

$$U^{\text{LJ}}(r) = 4\,\varepsilon \left[\left(\frac{\sigma}{r}\right)^{12} - \left(\frac{\sigma}{r}\right)^{6} \right] \tag{3.16}$$

ε (epsilon) is the depth of the potential well, σ (sigma) is the zero-crossing distance, and r denotes the scalar distance between the centers of two interacting particles i and j.

Since our MD simulations include electrostatic charges, we explicitly accounted for long-range interactions. A force is considered long-range when its spatial decay is slower than r^{-d}, where d is the dimensionality of the system. Two classic examples are the ion–ion charge–charge interaction, $v_{qq}(r) \propto r^{-1}$, and the molecular dipole–dipole interaction, $v_{\mu\mu}(r) \propto r^{-3}$ [128]. In order to calculate the long-range interactions we used Ewald summation method. The Coulomb potential between two particles with charges q_1 and q_2 separated by a distance r is:

$$U^{\text{Coulombic}}(r) = \frac{q_1 q_2}{4\pi\varepsilon_0\, r} \tag{3.17}$$

In MD simulations with periodic boundary conditions, this potential is effectively defined for all $r \geq 0$. Under such conditions the electrostatic sum does not converge, so one might be tempted to truncate the potential at a finite cutoff distance. For charged systems, however, an arbitrary cutoff introduces significant numerical errors. A standard solution

is the Ewald summation method. By introducing a convergence function and applying a Fourier transform, Ewald's approach splits the slowly, or conditionally, convergent lattice sum into rapidly converging parts. This lets us calculate the electrostatic forces very accurately and avoids the errors that simple cut-off methods cause [143].

$$v^{qq} = \frac{1}{2} \sum_{\mathbf{m}\in\mathbb{Z}^3}{}' \left(\sum_{i=1}^{N} \sum_{j=1}^{N} q_i q_j \left| \mathbf{r}_{ij} + \mathbf{m}L \right|^{-1} \right) \tag{3.18}$$

Here q_i and q_j are charges of particles i and j, respectively. The vector $\mathbf{m} = (m_x, m_y, m_z)$ runs over all integer triplets, $\mathbb{Z}^3$. For a cubic simulation box, $\mathbf{m}L$ locates the center of each periodic image. The prime on the outer sum indicates that the term with $i = j$ is excluded when $\mathbf{m} = \mathbf{0}$.

For understanding the energy calculation process through MD, we have to first analyze the Hamiltonian and the partition function of system for two different ensembles we used in our simulations, the NVT and NPT ensembles. Since the total energy can always be written as the sum of kinetic (dependent on p) and potential (dependent on q) contributions, the partition function factorizes into the product of a kinetic part and a potential part [128]. In the NVT ensemble, the partition function factorizes into ideal and excess contributions:

$$Q_{NVT} = \frac{1}{N!\, h^{3N}} \int d\mathbf{p}\; e^{-\mathcal{K}(\mathbf{p})/(k_{\mathrm{B}}T)} \int d\mathbf{q}\; e^{-\mathcal{U}(\mathbf{q})/(k_{\mathrm{B}}T)} = Q^{\mathrm{id}}_{NVT}\;\; Q^{\mathrm{ex}}_{NVT} \tag{3.19}$$

where

$$Q^{\mathrm{id}}_{NVT} = \frac{1}{N!\, h^{3N}} \int d\mathbf{p}\; e^{-\mathcal{K}(\mathbf{p})/(k_{\mathrm{B}}T)}, \qquad Q^{\mathrm{ex}}_{NVT} = \frac{1}{N!\, h^{3N}} \int d\mathbf{q}\; e^{-\mathcal{U}(\mathbf{q})/(k_{\mathrm{B}}T)}.$$

For a monoatomic ideal gas (setting $\mathcal{U} = 0$) the ideal part reduces to:

$$Q^{\mathrm{id}}_{NVT} = \frac{V^N}{N!\, \Lambda^{3N}}, \qquad \Lambda = \sqrt{\frac{h^2}{2\pi m\, k_{\mathrm{B}}T}} \tag{3.20}$$

including (Λ), the thermal de Broglie wavelength and Planck's constant (h) [128].

The excess partition function can be expressed in terms of the configurational integral:

$$Q_{NVT}^{\mathrm{ex}} = V^{-N} \int d\mathbf{r}\; e^{-\mathcal{V}(\mathbf{r})/(k_{\mathrm{B}}T)} = V^{-N}\, Z_{NVT} \tag{3.21}$$

$$Z_{NVT} = \int d\mathbf{r}\; e^{-\mathcal{V}(\mathbf{r})/(k_{\mathrm{B}}T)} \tag{3.22}$$

where Z_{NVT} is the standard configurational integral of the potential energy [128].

In the isothermal–isobaric ensemble the partition function is

$$Q_{NPT} = \frac{1}{N!\, h^{3N}\, V_0} \int_0^\infty dV \int d\mathbf{r}\, d\mathbf{p}\;\; \exp\Big[-\frac{H(\mathbf{r},\mathbf{p}) + P\,V}{k_{\mathrm{B}}T}\Big] \tag{3.23}$$

The Gibbs free energy follows as

$$G = -\,k_{\mathrm{B}}T\, \ln Q_{NPT} \tag{3.24}$$

Separating momentum and configuration integrals defines the configurational integral

$$Z_{NPT} = \int_0^\infty dV\, e^{-PV/(k_{\mathrm{B}}T)} \int d\mathbf{r}\; e^{-\mathcal{V}(\mathbf{r})/(k_{\mathrm{B}}T)} \tag{3.25}$$

Table 3.1 lists all the equations used in LAMMPS to compute physical properties during MD simulations [119].

Table 3.1: *Key thermodynamic quantities in MD simulations.*

Parameter	Equation	Description
Temperature (K)	$T = \frac{2E_{\text{kin}}}{N_{\text{DOF}} k_{\text{B}}}$ $E_{\text{kin}} = \sum_{i=1}^{N} \frac{1}{2} m_i v_i^2$ $N_{\text{DOF}} = dN - d - N_{\text{fix DOF}}$	From the equipartition theorem. E_{kin} is the total kinetic energy; N_{DOF} the active degrees of freedom (dN minus overall translation and constraints); k_{B} is Boltzmann's constant.
Kinetic energy	$E_{\text{kin}} = \sum_{i=1}^{N} \frac{1}{2} m_i v_i^2$	Sum of per-atom kinetic energies (m_i, v_i are the mass and velocity of atom i).
Potential energy	$E_{\text{pot}} = \sum_{\text{all interactions}} U$	Bonded and non-bonded potential energy as defined by the chosen force field.
Total energy	$E_{\text{tot}} = E_{\text{kin}} + E_{\text{pot}}$	Instantaneous total energy.
Pressure (atm)	$P = \frac{N k_{\text{B}} T}{V} + \frac{1}{dV} \sum_{i=1}^{N} \mathbf{r}_i \cdot \mathbf{f}_i$	Virial expression: ideal-gas term $N k_{\text{B}} T / V$ plus configurational (virial) term $(dV)^{-1} \sum_i \mathbf{r}_i \cdot \mathbf{f}_i$, where $\mathbf{r}_i$ and $\mathbf{f}_i$ are the position and force on atom i.

3.3 Permeation Models for Gas separation in Polymer/ZIF-8 Composites

In gas permeation through MMMs, three primary phases must be considered: the dispersed filler phase, the continuous polymer matrix, and the interfacial region between them [144, 145, 146]. Many models that expand on this idea have been created so far [147, 148, 149, 150]. In this thesis, we employ both the Maxwell (Eq. (3.26)) [36] and the Modified Felske (Eq. (3.27)) [37] models to examine how the interfacial region between PIM-1 and ZIF-8 influences gas permeation of the MMM. The models are as follows:

$$P_r \;=\; \frac{P}{P_m} \;=\; \frac{2\,(1-\phi) \;+\; (1+2\phi)\,\lambda_{dm}}{(2+\phi) \;+\; (1-\phi)\,\lambda_{dm}} \tag{3.26}$$

where (P_r) is the relative permeability of the species, (P) is the effective permeability in

the MMM, (P_m) is the permeability in the continuous polymer matrix (PIM-1), (ϕ) is the volume fraction of the filler particles, and $\lambda_{dm} = P_d/P_m$ is the permeability ratio, with (P_d) denoting the permeability in the dispersed filler phase.

$$P_r = \frac{P}{P_m} = \frac{1 + 2\left(\frac{\beta-\gamma}{\beta+2\gamma}\right)\phi}{1 - \left(\frac{\beta-\gamma}{\beta+2\gamma}\right)\phi\,\psi} \tag{3.27}$$

$$\beta = (2+\delta^3)\,\lambda_{dm} - 2\,(1-\delta^3)\,\lambda_{lm} \tag{3.28}$$

$$\gamma = 1 + 2\,\delta^3 - (1-\delta^3)\,\lambda_{dl} \tag{3.29}$$

$$\psi = 1 + \left(\frac{1-\phi_m}{\phi_m^2}\right)\phi \tag{3.30}$$

where δ is the ratio of the outer-interface radius to the core radius of ZIF-8, ϕ is the volume fraction of the ZIF-8 particles (i.e. the total volume fraction of the dispersed phase, comprising core filler particles plus their interfacial layers), P_I is the permeability in the interfacial zone, P_d is the permeability in the core filler particles, and P_m is the permeability in the continuous polymer matrix. The corresponding permeability ratios are $\lambda_{dm} = P_d/P_m$, $\lambda_{Im} = P_I/P_m$, and $\lambda_{dI} = P_d/P_I$. Here, β and γ are defined by Eq. (3.28) and Eq. (3.29), respectively, and ψ is given by Eq. (3.30) as a function of ϕ_m (the maximum packing fraction of the ZIF-8 particles). According to these equations, the Maxwell model treats the MMM as an ideal mixture, neglecting the influence of interfacial voids on gas permeability. In contrast, the modified Felske model explicitly accounts for these voids. We applied both models to quantify the void effect numerically.

3.4 Cementitious Composites

In cementitious composite systems the simulations started with constructing sandwich-like structures made of rubber and CSH. Rubber Hydrocarbon (RH) makes up 45.2% of the rubber particles and consists of repeating cis-1,4-isoprene units [17]. Therefore, we

built an RH model to represent the rubber system in this study. The computational workflow of the first part of the thesis is shown in Figure 3.1.

Figure 3.1: *Computational workflow of cementitious composite systems.*

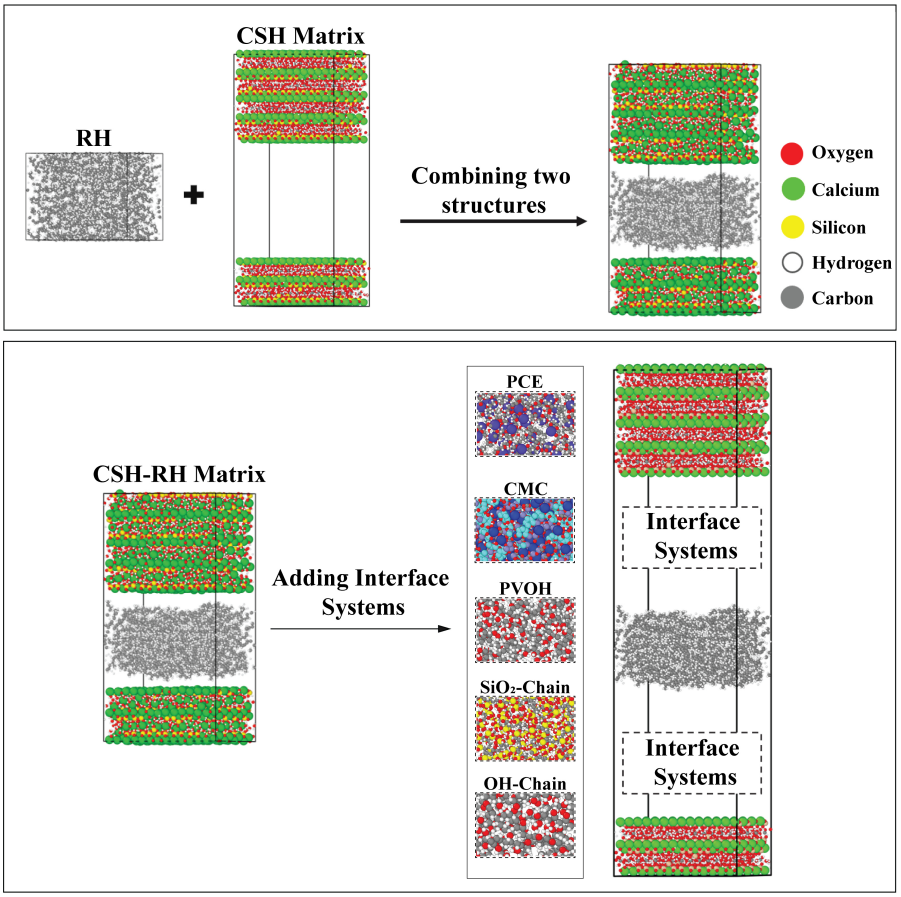

Several polymeric interfacial agents are introduced to effectively bridge the gap between the hydrophilic surface of CSH and the hydrophobic surface of RH. These interfacial polymers were, PCE, CMC, and PVOH. We also constructed separate atomistic carbon-chain models and systematically functionalized them with hydroxyl (–OH) and silica (SiO_2) groups to evaluate how each group acts as a bridge between CSH and RH.

Since CSH is the main gelling component formed during cement hydration, its atomic structure was employed in this study to represent concrete within our molecular simulations [151, 152]. The CSH atomistic model was constructed using the ClayFF [153]

force field and the simulation box had dimensions of $51.73\,\text{Å} \times 22.3174\,\text{Å} \times 68.31\,\text{Å}$, with angles $\alpha = 90°$, $\beta = 90°$, and $\gamma = 56.49°$, and tilt factors $xy = 14.766\,\text{Å}$, $xz = yz = 0$ containing 8,593 atoms. The initial atomistic configurations of RH, PCE, and the functionalized carbon chains were built using MS software. Subsequently, these configurations were converted into formats compatible with LAMMPS [119] using the msi2lmp [120] package. Finally, a 21-step [154] MD simulation protocol was performed on these polymer systems individually. The molecular models of CMC and PVOH polymers were adapted from previously published study [155]. Since the CSH model was constructed with a triclinic simulation box, all polymer systems, including RH and the interfacial polymers, were deformed in the xy plane to match the same triclinic geometry for consistency, during which their simulated densities were consistently monitored and validated against experimental density values to ensure accuracy.

The 21-step MD equilibration protocol in Table 3.2 was adapted from Ref. [154]. As the table shows, the simulations proceeded in cycles with progressively higher temperatures and pressures.

Table 3.2: *21-step MD equilibration scheme.*

Step	Ensemble	Conditions	Length (ps)
1	NVT	$T_{\max}$	50
2	NVT	T_{final}	50
3	NPT	$T_{\text{final}},\ 0.02 \times P_{\max}$	50
4	NVT	$T_{\max}$	50
5	NVT	T_{final}	100
6	NPT	$T_{\text{final}},\ 0.6 \times P_{\max}$	50
7	NVT	$T_{\max}$	50
8	NVT	T_{final}	100
9	NPT	$T_{\text{final}},\ P_{\max}$	50
10	NVT	$T_{\max}$	50
11	NVT	T_{final}	100
12	NPT	$T_{\text{final}},\ 0.5 \times P_{\max}$	5
13	NVT	$T_{\max}$	5
14	NVT	T_{final}	10
15	NPT	$T_{\text{final}},\ 0.1 \times P_{\max}$	5
16	NVT	$T_{\max}$	5
17	NVT	T_{final}	10
18	NPT	$T_{\text{final}},\ 0.01 \times P_{\max}$	5
19	NVT	$T_{\max}$	5
20	NVT	T_{final}	10
21	NPT	$T_{\text{final}},\ P_{\text{final}}$	800

3.4.1 Details of Molecular Simulations of CSH/RH/PCE Composites

- **Modeling of RH Polymer** The Consistent Valence Force Field (CVFF), known for its reliability in simulating organic systems based on prior research [17, 156, 157, 158] was selected to model RH polymer, which consists of 40 repeating monomer units. To create the initial configuration of polymer chain we used MS program. Then, by using the LAMMPS [119] software, the 10 RH polymer chains were initially packed and equilibrated through equilibrium MD simulations across 21-steps method [154]. To confirm that the system had reached thermodynamic equilibrium, we ran an additional 1 ns simulation in the NVT ensemble at 300 K, employing a 1 fs integration timestep. The equilibrated RH simulation box had dimensions $51.7\,\text{Å} \times 22.3\,\text{Å} \times 43.47\,\text{Å}$, with angles $\alpha = 90°$, $\beta = 90°$, and $\gamma = 56.49°$, and the system contained 5,220 atoms. The validation of our model was confirmed by the RH density, consistently matching the literature-reported value of $0.90\,\mathrm{g/cm^3}$ [159].

- **Modeling of PCE Polymer** The PCE was modeled as the interface polymer between CSH and RH. PCE is a polymer-based compound obtained from methoxy-polyethylene glycol copolymer which has been widely used as a superplasticizer in the cement industry for years [160]. The core structure of PCE consists of two distinct repeating units (Figure 3.2(b)): acrylic acid (AA) sodium salt and isopentenyl polyethylene glycol (TPEG), with a molar ratio of 4:1 between acid and ether components. The side chains were evenly distributed along the polymer backbone, with a total number of 10 side chains (denoted as 'c') and a degree of polymerization (d) of 12 [161]. The force field used in this simulation was the CVFF force field [158]. First, we built three chains of PCE for the interface of CSH/RH system in MS program. Then, like the RH model, we used the 21-step equilibrium simulation

protocol. At the end of the simulation, we observed the full compaction of the three chains. To ensure that the entire system achieved thermodynamic equilibrium, an additional 1 ns simulation was conducted within the NVT ensemble at 300 K, employing a 1 fs integration timestep. The simulation box dimensions for the PCE model were $a = 51.70\,\text{Å}$, $b = 26.73\,\text{Å}$, and $c = 37.04\,\text{Å}$, with angles $\alpha = 90°$, $\beta = 90°$, and $\gamma = 56.49°$, and the system contained 4,140 atoms. The molecular weights of PCE range from 9000 to 33,000 g/mol [161]. This aligns well with the molecular weight of our synthesized PCE polymer, which is 10099.72 g/mol validating the accuracy of our model [161].

Figure 3.2: *Structures of (a) RH and (b) PCE monomers.*

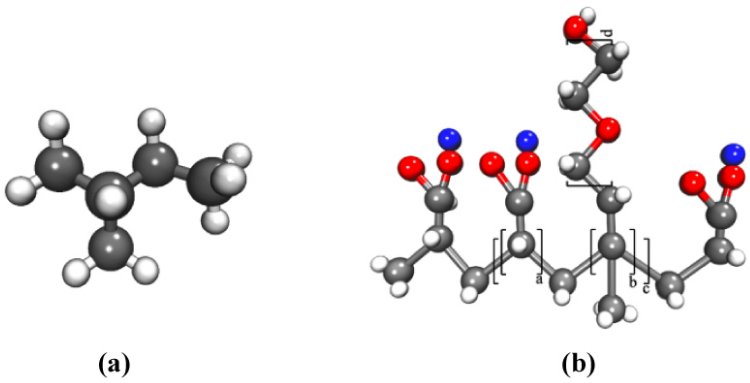

(a) **(b)**

- **Modeling of CSH/RH/PCE Composite**

  Initially, an empty space was created within the CSH model to accommodate the polymer layers. The RH model was first inserted into the CSH matrix. Subsequently, the PCE polymer was embedded within the RH/CSH model from both the top and bottom sides of the RH to monitor its interaction potential between the rubber and CSH. After completing the embedding process of RH and PCE inside

the CSH, 21-step [154] MD simulations was conducted along the z-axis direction, resulting in a compacted composite with lattice cell parameters of $a = 51.7\,\text{Å}$, $b = 22.3\,\text{Å}$, $c = 181.37\,\text{Å}$, and angles $\alpha = \beta = 90°$, $\gamma = 56.49°$. The final composite consisted of 22,093 atoms. Finally, to ensure the system was fully equilibrated and to obtain trajectory information, an additional 1 ns simulation in the NVT ensemble was performed at 300 K.

Figure 3.3: *Structures of CSH/RH and CSH/RH/PCE composites.*

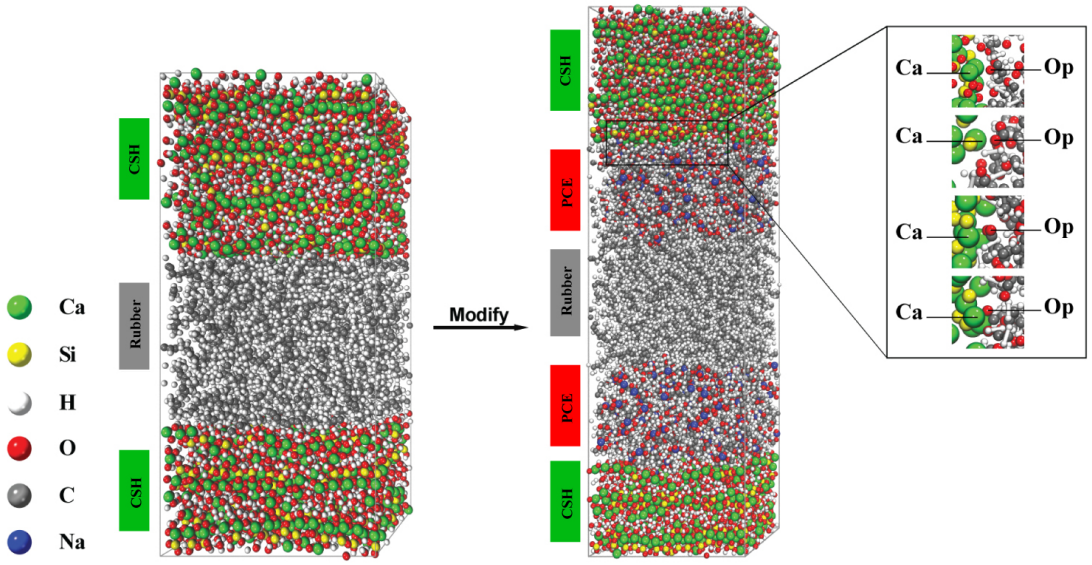

3.4.2 Details of Molecular Simulations of CSH/RH/Binder Composite

The molecular models of CMC and PVOH polymers, which are known as binder polymers, were adapted from previously published study [155]. After deforming them in the xy plane with a tilt factor of $xy = 14\,\text{Å}$, their dimensions were as follows: for the CMC system, the simulation box dimensions were $51.70\,\text{Å} \times 22.30\,\text{Å} \times 36.74\,\text{Å}$, with angles $\alpha = 90°$, $\beta = 90°$, and $\gamma = 56.49°$, containing 3,130 atoms; and for the PVOH system, they were $51.70\,\text{Å} \times 22.30\,\text{Å} \times 55.14\,\text{Å}$, with angles $\alpha = 90°$, $\beta = 90°$, and

$\gamma = 56.49°$, containing 7,176 atoms. Just like the CSH/RH/PCE prcocess, to create the composite structures, we initially modified the CSH model by introducing a void to facilitate the insertion of the polymer layers. The process began by inserting the rubber model into the CSH matrix. Subsequently, polymer layers of CMC or PVOH were added separately on both the top and bottom sides of the rubber layer. This arrangement facilitated a thorough investigation of how these polymers interact with the CSH matrix. Once the polymer layers were embedded, we conducted 21-step [154] MD simulations along the z-axis to compact the composite structure (Figure 3.4). Following this, a 1 ns NVT simulation at 300 K was performed to achieve thermal equilibration and to collect trajectory data for further analysis.

Figure 3.4: *Simulation models of CSH/RH/CMC composite and CSH/RH/PVOH composite.*

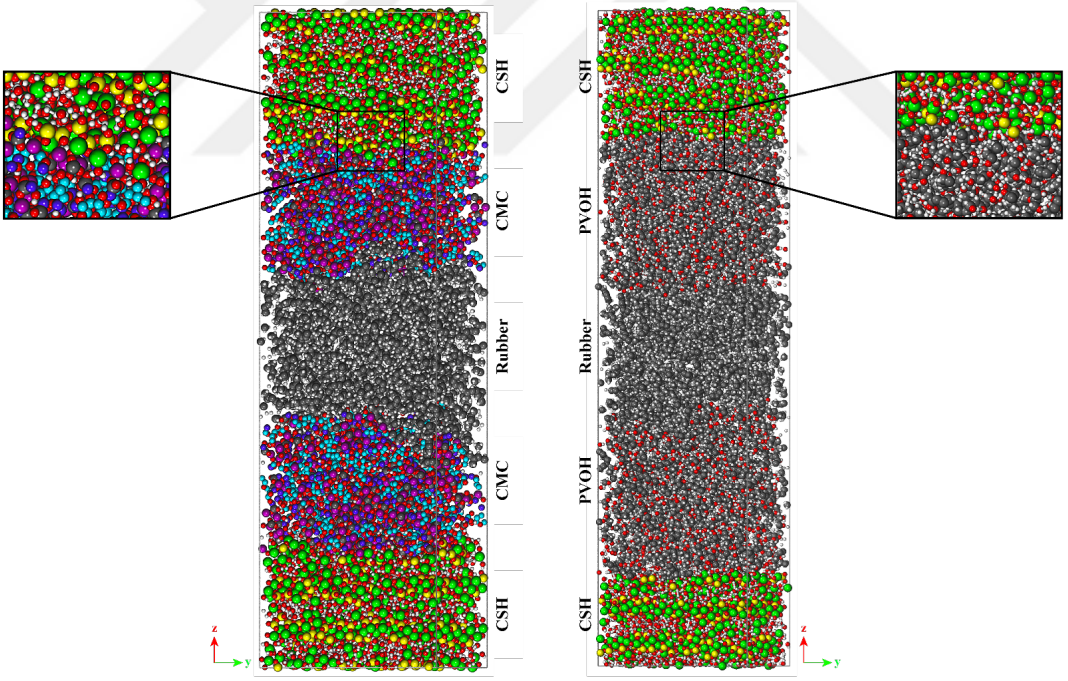

3.4.3 Details of Molecular Simulation of CSH/RH/Carbon chains

To create the carbon chains, saturated hydrocarbon chains containing 51 backbone carbon atoms were first generated using the polymerization tool in MS program. Subsequently, two functional groups including (–OH) and (SiO_2) were introduced by substituting approximately half of the hydrogen atoms along the hydrocarbon backbone. This substitution ensured a homogeneous distribution of the functional groups across the length of each carbon chain, as illustrated in Figure 3.5. Then, ten chains of each functionalized carbon chain were placed into individual simulation boxes. The pairwise LJ potential parameters, bond, angle, dihedral, and improper parameters were assigned from the CVFF force field using the msi2lmp package. Finally, a 21-step simulation process [154] was performed to compact the functionalized carbon chain systems. The equilibrated simulation boxes had the following dimensions: for the OH-functionalized carbon chains, the simulation box measured $51.70\,\text{Å} \times 22.30\,\text{Å} \times 14.576\,\text{Å}$, with angles $\alpha = 90°$, $\beta = 90°$, and $\gamma = 56.49°$, containing 1,810 atoms. For the SiO_2-functionalized carbon chains, the simulation box measured $51.70\,\text{Å} \times 22.30\,\text{Å} \times 28.48\,\text{Å}$, with angles $\alpha = 90°$, $\beta = 90°$, and $\gamma = 56.49°$, containing 3,110 atoms. The resulting compacted chains were then embedded within the CSH and RH matrix (Figure 3.6).

Figure 3.5: *Functionalization of carbon chains: (a) carbon chain, (b) SiO_2–carbon chain, (c) OH–carbon chain.*

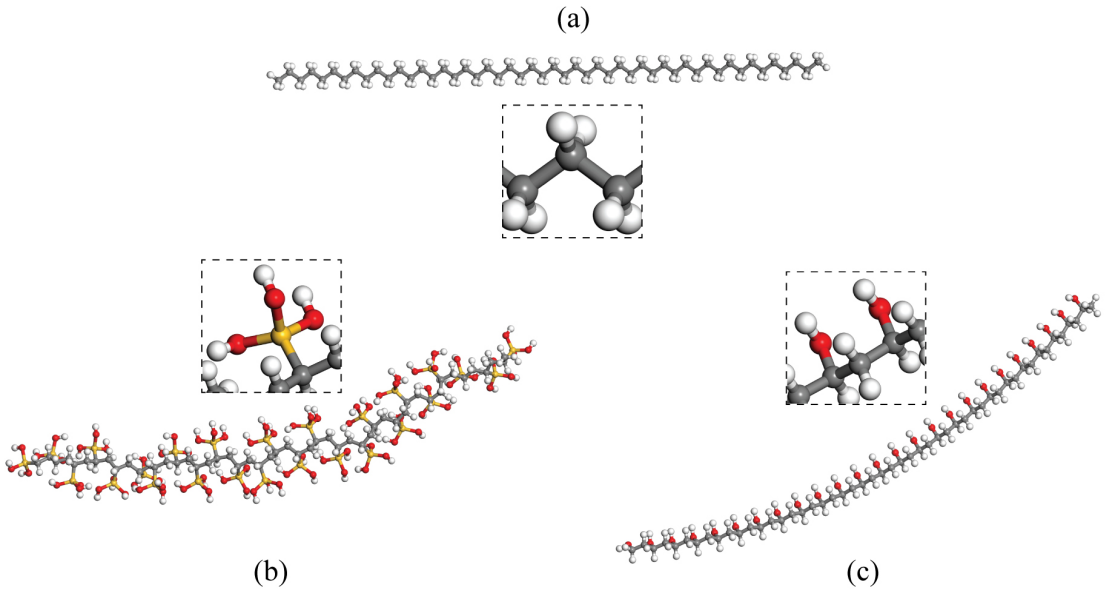

Figure 3.6: *CSH/RH/carbon chain composites: (a) CSH/RH/OH-functionalized carbon chain composite, (b) CSH/RH/SiO_2-functionalized carbon chain composite.*

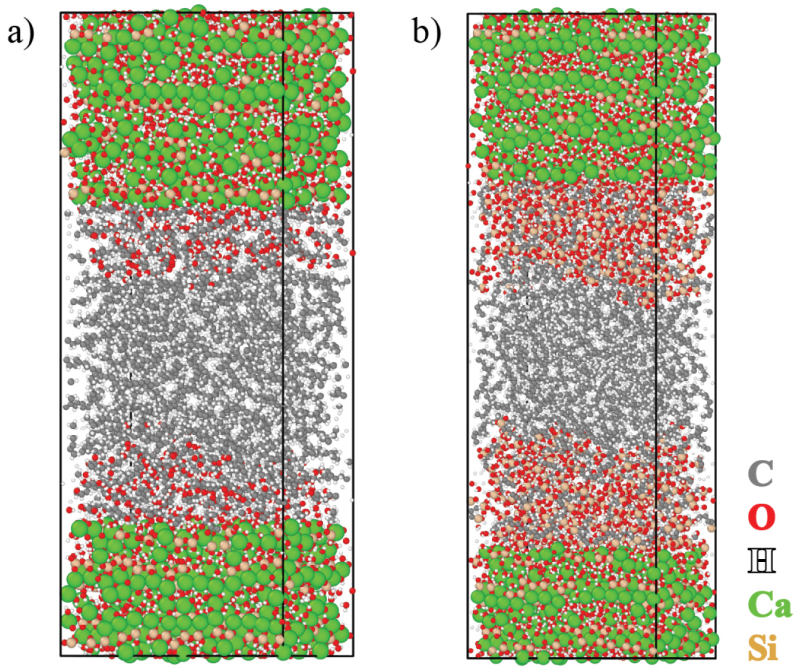

3.5 Polymer/ZIF-8 Composites

We started with constructing ZIF-8 membranes using two structural forms: (1) the pristine crystalline structure (cryZIF-8) and (2) ZIF-8 structure obtained via pressure-induced amorphization at 0.4 GPa (aZIF-8@0.4GPa) [162]. These two structures were used as the starting points for all subsequent modelling. The computational workflow of the second part of the thesis is shown in Figure 3.7.

Figure 3.7: *Computational workflow to predict gas permeabilities in ZIF-8/PIM-1 MMMs.*

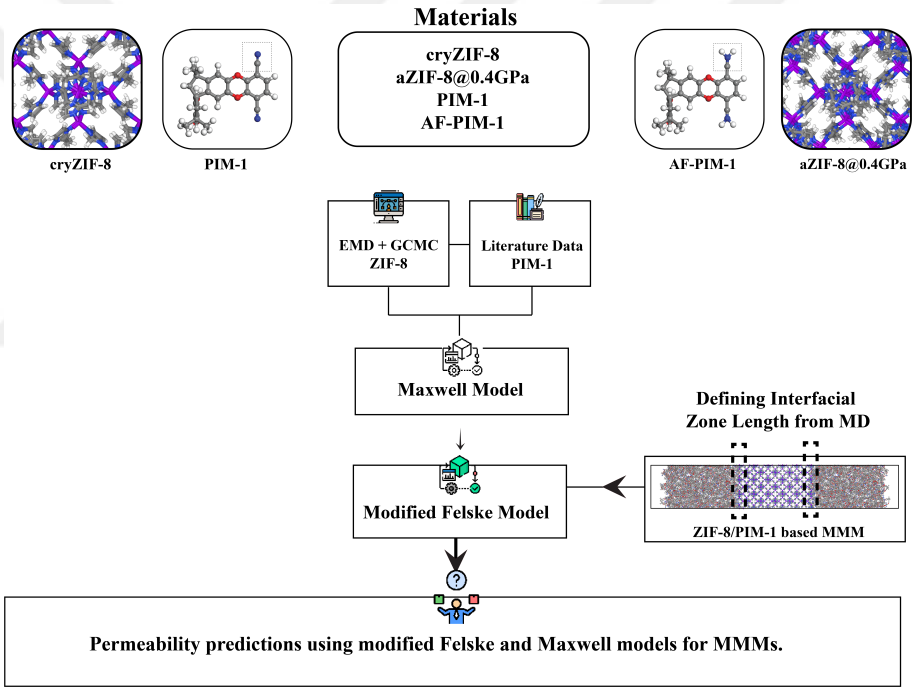

To create a ZIF-8 membrane model, the ZIF-8 structure was first duplicated along the z-direction. This step was required to match the dimensions of ZIF-8 and the PIM-1 polymer in the z-direction. Afterwards, to break periodicity along the z-axis, the outermost Zn atoms were removed, and the remaining N atoms were terminated with H atoms (Figure 3.8). The particles of ZIF-8 structures were parameterized with the

ZIF-FF force field [163] and PACMOF charges [164]. Finally, the membrane structures were relaxed by a 1 ns equilibrium run in the NVT ensemble at room temperature using LAMMPS [119] package. Both equilibrated simulation boxes were orthogonal, each containing 13,716 atoms. For cryZIF-8, the simulation box dimensions were $50.9702\,\text{Å} \times 50.9702\,\text{Å} \times 101.9404\,\text{Å}$. For aZIF-8@0.4 GPa, the simulation box dimensions were $50.013\,\text{Å} \times 50.041\,\text{Å} \times 99.818\,\text{Å}$.

Figure 3.8: *ZIF-8 membrane model.*

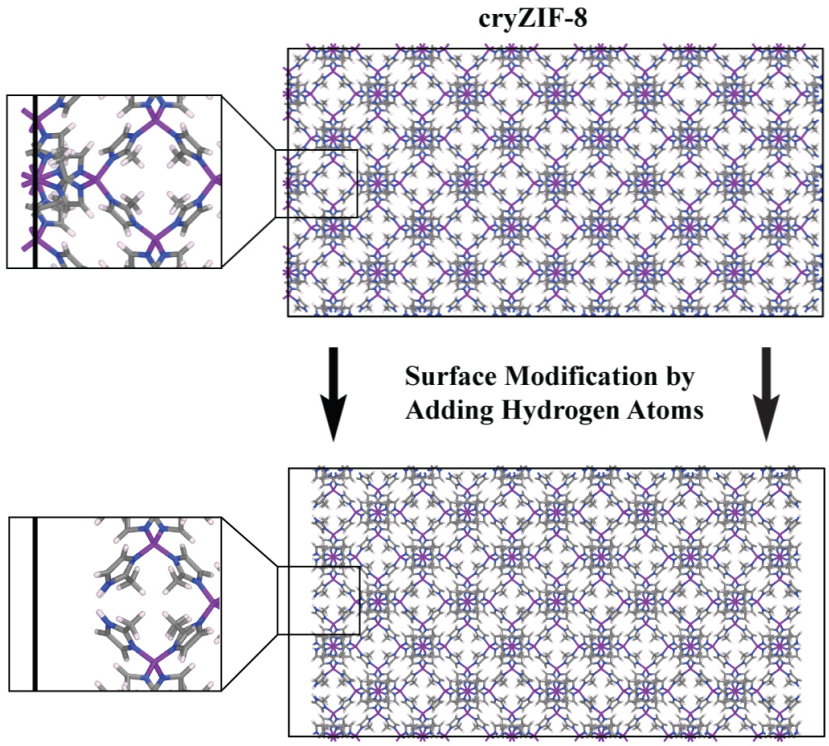

- **Developing PIM-1 polymer membrane** Two PIM-1 membrane models were prepared: pure PIM-1 polymer and AF-PIM-1 polymer. Both models were taken from a previously published study [165]. The coordinate and topology files were then converted from GROMACS format to LAMMPS-compatible input files. Bond, angle, and dihedral parameters were assigned with the DREIDING force field [166],

as reported in the literature [165]. Both the PIM-1 and AF-PIM-1 systems were orthogonal. The PIM-1 simulation box measured 50.9701 Å$\times 50.9703$ Å$\times 117.6757$ Å and contained 19,800 atoms. The AF-PIM-1 simulation box measured 50.9409 Å $\times$ 50.9588 Å $\times$ 101.8480 Å and contained 18,900 atoms.

- **Developing ZIF-8/PIM-1 MMMs** The ZIF-8/PIM-1 based MMM model was generated by first placing PIM-1 and ZIF-8 in a simulation box and then subjecting the system to a 21-step [154] compression–equilibration protocol along z-axis direction. This procedure allowed the PIM-1/ZIF-8 interface to develop naturally and uniformly (Figure 3.9(a)). After a 1 ns NVT with 1 fs timestep equilibration for the compacted system, the entire box was replicated along the z-axis direction, producing a final configuration in which the ZIF-8 phase lay at the center, sandwiched by PIM-1 layers on both sides (Figure 3.9(b)). Non-bonded interactions were truncated at 12.50 Å, and long-range electrostatics were evaluated with Ewald summation at a relative accuracy of 10^{-4}. Polymer–ZIF interactions were represented as the Coulombic and LJ terms, with cross parameters obtained from the Lorentz–Berthelot mixing rule [167, 168]. The same workflow was applied to four MMM systems: (i) crystalline ZIF-8 with pure PIM-1, (ii) crystalline ZIF-8 with AF-PIM-1, (iii) under pressure aZIF-8@0.4GPa with pure PIM-1, and (iv) under pressure aZIF-8@0.4GPa with AF-PIM-1.

Figure 3.9: *ZIF-8/PIM-1-based MMMs. Equilibrated membrane structure (a) before replicating, (b) after replicating.*

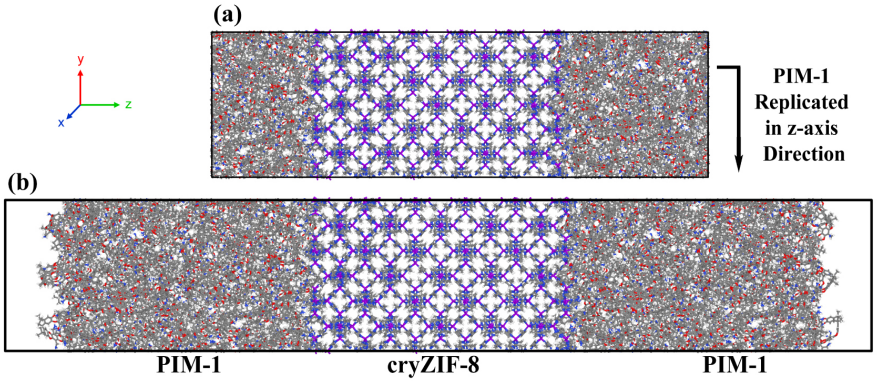

3.6 Property Analysis

3.6.1 RDF

To describe the spatial correlation between atoms on the surfaces of two materials, the RDF analysis was employed. This function characterizes the system's microstructural information and reflects the interactions between particles [169, 170]. It also provides insight into the structural organization and interactions within the system. The RDF analysis describes how the local density of matter changes with distance from a reference point and quantifies the frequency of specific inter-particle separations [171]. In a crystalline solid, the RDF curve exhibits pronounced peaks, each corresponding to an interatomic distance that recurs throughout the lattice. During MD simulation, the RDF is computed by counting the number of atomic pairs whose separations fall within successive distance bins. This histogram is then normalized to the system's average number density, yielding the mean atomic density as a function of radial distance. The general expression to calculate the RDF (g(r)) is:

$$g(r) = \frac{\mathrm{d}N}{4\pi r^2 \, \rho \, \mathrm{d}r} \tag{3.31}$$

where r is the distance between particles, N is the number of particles, and ρ is the average density of the system [170]. After calculating the RDF in our simulations, we plotted it with the radial distance from the reference atom on the x-axis (up to the non-bonded cut-off) and the RDF value g(r) on the y-axis. To explore how the interface polymer interacts with the composite matrix, we calculated the RDF for the relevant pairs of atoms. High peaks in the RDF plot show that atoms in the interface polymer and the matrix are close to one another, confirming strong interaction and indicating that the test was successful.

3.6.2 Calculation of Interfacial Adhesion Energy

The interfacial adhesion energy is an important parameter that indicates the interaction at the interface [17, 172]. In this thesis, the interfacial adhesion energy between the filler and the polymer matrix was calculated by subtracting the final energies of the individual composite components from the final energy of the entire composite system. This method was adapted from approaches reported in previous studies [17, 172] with slight modifications. In this study, adhesion energy values are reported as representative (qualitative) indicators; their absolute magnitudes may vary with simulation box size. All energy values were represented using the total energy (kcal/mol) of the system. The equations used to calculate the adhesion energies of (a) CSH/RH/Polymer interfaces and (b) ZIF-8/PIM-1 composites are presented in Equations (3.2) and (3.3), respectively.

$$\Delta E = E_{\text{total}}^{\text{Composite}} - E_{\text{total}}^{\text{RH}} - E_{\text{total}}^{\text{CSH}} - E_{\text{total}}^{\text{Interfacial Polymer}} \tag{3.32}$$

$$\Delta E = E_{\text{total}}^{\text{MMM}} - E_{\text{total}}^{\text{ZIF-8}} - E_{\text{total}}^{\text{PIM-1}} \tag{3.33}$$

3.6.3 S-order Parameter

We computed the orientational s-order parameter for the RH layer before and after adding interfacial polymers to the CSH/RH composite to assess whether the RH layer lost elasticity. We used the change in s-order as our metric, because it represents the degree of molecular alignment [173]. We have calculated it based on the following equation:

$$P_2(\cos\beta) = \frac{1}{2}\left(3\cos^2\beta - 1\right) \tag{3.34}$$

where β is the angle between a molecule's long axis and the director. The s-order coefficient, $\langle P_2 \rangle$, varies between $-\frac{1}{3}$ and 1. For a perfectly narrow distribution aligned parallel to the symmetry axis, $\langle P_2 \rangle = 1$. For an isotropic distribution, $\langle P_2 \rangle = 0$. In contrast, for a distribution in which all orientations are perpendicular to the symmetry axis, $\langle P_2 \rangle = -\frac{1}{3}$.

4. RESULTS AND DISCUSSION

4.1 Models Dimensions

To evaluate whether the model dimensions are sufficient to analyze the interfacial behaviour for composite systems, we calculated one-dimensional mass density profiles along the z-axis direction, $\rho(z)$, for all components in both composite groups (CSH/RH-based and ZIF-8/PIM-1-based composites). The densities were determined by binning the atoms along the z-axis direction and averaging over the production trajectory by MD simulations. We considered the model's simulation box dimensions to be sufficient if each slab had a central flat region in $\rho(z)$ that matched the corresponding experimental density within the error bars. In the cementitious composites (Figures 4.2(c) and 4.4), CSH and the polymer systems, including rubber and interfacial polymers, have flat regions away from the interfaces, so they behave more like bulk-like regions than thin interphases. In the ZIF-8/PIM-1 MMM (Figure 4.8), PIM-1 on both sides of ZIF-8 shows long, flat areas whose densities are consistent with experimental data. Therefore, the polymer region is thick enough and has a density corresponding to the experimental value. These density profiles show that each phase contains a bulk-like interior, and interface effects appear only near the contacts. Therefore, the chosen box dimensions are sufficient to study both systems.

4.2 CSH/RH/PCE Composite

In the CSH/RH/PCE composite, we computed RDFs to assess the interfacial bonding improvement expected from the PCE polymer. In our models, the calcium ions (Ca^{2+}) positioned on the surface of the CSH structure are the primary candidates for pairwise interactions with polymers due to their 2+ charge. Therefore, the interaction of these ions with rubber and PCE was compared via the RDF curves (Figure 4.1(a)). The black line indicates the interaction between Ca^{2+} ions in CSH and the oxygen atoms of the PCE, while

the red and blue lines represent the interactions between Ca^{2+} ions and carbon (CR) and hydrogen (HR) atoms in the rubber, respectively. In the CSH/RH system, the RDF profiles for Ca-CR and Ca-HR interactions do not display any specific characteristics peaks. This observation supports the conclusion that there is a lack of significant interaction between RH and CSH. While g(r) diagram representing the Ca-O interaction in the CSH/RH/PCE system, exhibits prominent peaks at distances around 4 Å, these peaks indicate a strong interaction between the Ca^{2+} ions and the oxygen atoms in the PCE, which is expected due to the polar nature of the PCE molecules enhancing the bonding with Ca^{2+} ions. This enhanced interaction suggests that the incorporation of PCE as an interfacial layer in the CSH/RH system leads to improved bonding and structural integration, which can enhance the mechanical properties and stability of the composite material. The visualization of these atomic interactions is shown in Figure 4.1(a).

To measure the degree of orientational order of rubber in two systems of CSH/RH and CSH/RH/PCE composites, the s-order parameter (Eq. (3.34)) for these systems was analyzed over a 1 ns MD simulations in NVT ensemble (Figure 4.1(b)). The data show that the S-order parameter for both systems remains closely aligned, with fluctuations around an average value of approximately 0.338. The similar S-order parameters show that the rubber chains keep the same orientation and alignment, and therefore the same elasticity, in both systems. In other words, adding PCE polymer to the CSH/RH matrix does not change the orientational order of the rubber molecules.

The z-density profile for CSH/RH/PCE composite system is shown in Figure 4.2(c). This profile illustrates the density distribution along the z-axis, providing a valuable insight into the extent of rubber embedding within the CSH matrix and the PCE interface. In the CSH/RH system the embedded length of rubber inside the CSH is observed to be 5 Å from the bottom of the rubber layer and 2 Å from the top. This indicates a relatively

Figure 4.1: *(a) RDF analysis for comparing the interaction between Ca^{2+} ions in CSH with O atoms of PCE, and with C and H atoms of RH, (b) variation of s-order parameter during MD simulations for RH system in both CSH/RH and CSH/RH/PCE composites.*

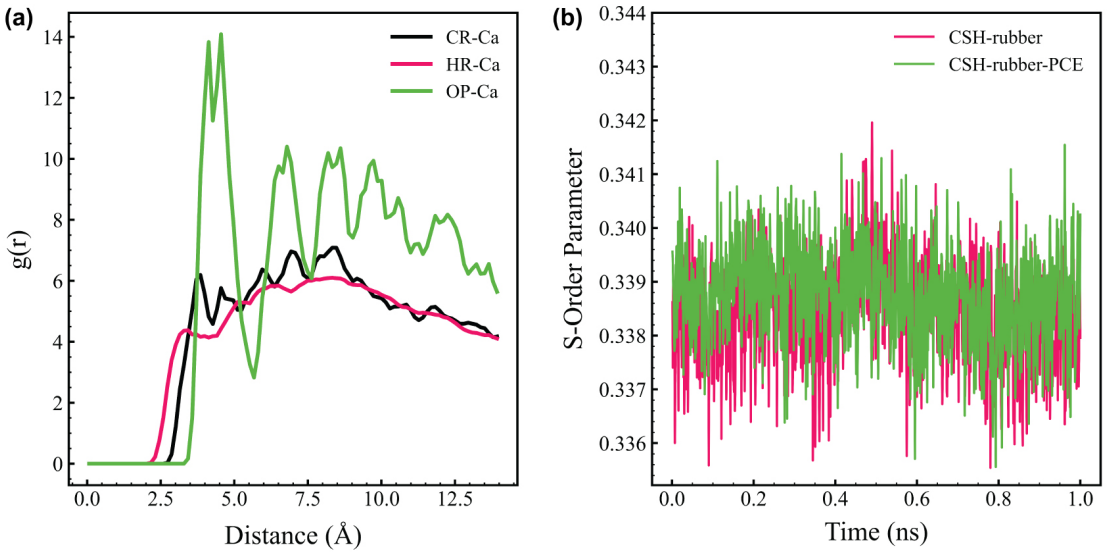

limited penetration of the rubber into the CSH matrix, resulting in a less extensive interaction between the two components. Conversely, in the CSH/RH/PCE system, the rubber is embedded within the PCE interface to a greater extent, with an embedding depth of 10 Å from both the top and bottom of the rubber layer. This increased embedding length signifies a more pronounced interaction between the rubber and the PCE, facilitated by the interfacial properties of the PCE. The enhanced embedding of rubber within the PCE interface suggests an improvement in the composite material's structural integrity. The greater interfacial interaction can lead to better stress transfer and adhesion between the rubber and the surrounding CSH matrix, potentially resulting in improved mechanical properties of the composite. This improvement is critical for applications requiring robust and durable materials, as it enhances the overall performance of the composite by ensuring stronger interfacial bonding and better load distribution across the components.

One of the essential criteria for assessing the compatibility of a composite is the

evaluation of its interfacial adhesion energy. The interfacial adhesion energy is primarily composed of the van der Waals interaction energy (E_{VDW}) and Coulomb interaction energy (E_{Coul}). Figure 4.2(a). illustrates the comparative analysis of the interfacial energy between CSH/RH and CSH/RH/PCE. To calculate the interfacial adhesion energy in the CSH/RH and CSH/RH/PCE systems at equilibrium, the total van der Waals and Coulombic interaction energy ($E_{\text{VDW-Coul}}$) were determined by summing the van der Waals (E_{VDW}) and Coulombic (E_{Coul}). The change in energy (ΔE) due to the introduction of components was calculated using the formula:

$$\Delta E = \left(E_{\text{vdW+Coul}}\right)_{\text{CSH/RH/PCE}} - \left(E_{\text{vdW+Coul}}\right)_{\text{RH}} - \left(E_{\text{vdW+Coul}}\right)_{\text{CSH}} - \left(E_{\text{vdW+Coul}}\right)_{\text{PCE}} \quad (4.1)$$

Using this approach, the $E_{\text{VDW-Coul}}$ for the CSH/RH system was determined to be -79947.9 kcal/mol. After the addition of the PCE polymer, this value increased to -85788.09 kcal/mol (minimum energy), indicating a 7.3% increase in the total interaction energy. This increase can be attributed to the role of PCE polymer in system, facilitating stronger molecular interactions between the CSH and RH components. The incorporation of PCE can introduce additional binding sites, leading to a more effective distribution of stress and an improvement in the mechanical stability of the composite.

Figure 4.2: *(a) Comparison of vdW-Coulomb adhesion energy between CSH/RH and CSH/RH/PCE systems, (b) Illustration of the interface zone; (c) z-density plot of the CSH/RH/PCE composite.*

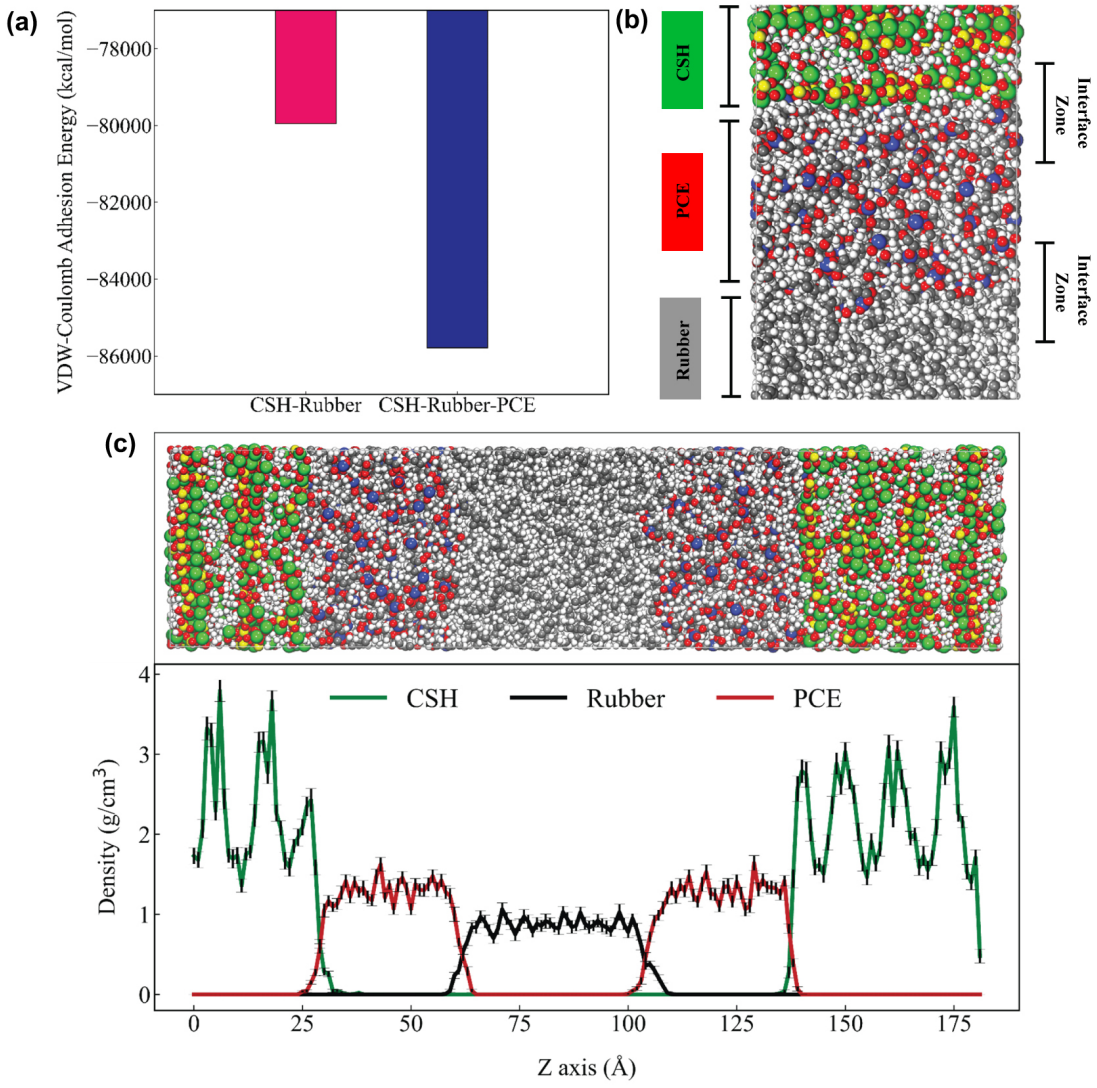

4.3 CSH/RH/Binder Composite

The first criteria analyzed for assessing the compatibility between several layers of a composite is the evaluation of the interfacial adhesion energy between its consisting layers. To do so, the adhesion energies of CSH/RH/CMC and CSH/RH/PVOH composites were calculated based on the following equation:

$$\Delta E = (E_{\text{total}})_{\text{Composite}} - (E_{\text{total}})_{\text{Rubber}} - (E_{\text{total}})_{\text{CSH}} - (E_{\text{total}})_{\text{Binder Polymer}} \tag{4.2}$$

According to Figure 4.3(a), the adhesion energy for the CSH/RH/PVOH system is -4559.24 kcal/mol and for CSH/RH/CMC system is -5337.85 kcal/mol (minimum energy) indicating a 17.08% increase in the total interaction energy. This increase can be attributed to the fact that CMC is a water-soluble polymer and can interact easily with the hydrophilic part of the composite, CSH. So, it acts as an efficient bridge connecting CSH and RH together to solve the incompatibility between them. The incorporation of CMC can introduce additional binding sites, leading to a more effective distribution of stress and an improvement in the mechanical stability of the composite.

Figure 4.3: *(a) Comparison of total adhesion energy between CSH/RH/CMC and CSH/RH/PVOH systems, (b) Comparing RDF plots of CSH/RH and CSH/RH/CMC composite systems.*

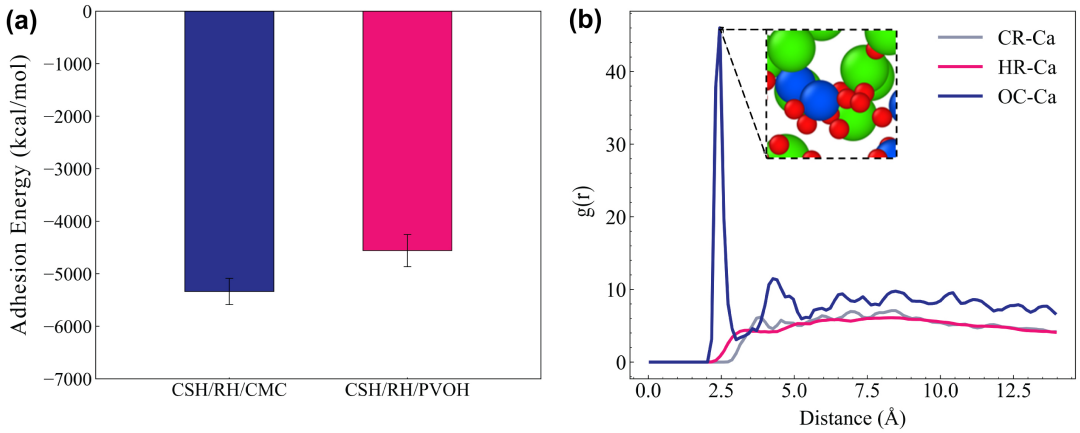

To describe the spatial correlation between atoms on the surfaces of two materials,

the RDF analysis is mainly used. In our study, we conducted an RDF analysis to compare the interatomic interactions between the CMC polymer and the CSH matrix with those between the RH polymer and the CSH matrix. Ca^{2+} ions on the surface of the CSH structure, with their 2+ charge, are the main candidates for pairwise interactions with the atoms of polymers. In the RDF plots (Figure 4.3(b)), the blue line represents the interaction between Ca^{2+} ions in CSH and the oxygen atoms of CMC. The gray and pink lines show the interactions between Ca^{2+} ions and the carbon (CR) and hydrogen (HR) atoms in the rubber, respectively. In the CSH/RH system, the RDF profiles for Ca-CR and Ca-HR interactions do not show any distinct peaks. This indicates that there is minimal significant interaction between isoprene and CSH. In contrast, the RDF plot for the CSH/RH/CMC system reveals a pronounced peak around 2.45 Å for the Ca-O interaction. This peak signifies a strong interaction between the calcium ions and the oxygen atoms in CMC. The enhanced interaction suggests that incorporating CMC as an interfacial layer in the CSH/RH system improves bonding and structural integration, which likely enhances the mechanical properties and stability of the composite material.

The next criterion is analyzing the density of composites in the z direction to visualize the embedment of rubber within the composites. As shown in Figure 4.4, the rubber layer in the CSH/RH/CMC composite is embedded homogeneously within the composite matrix. This demonstration suggests that the voids between the rubber and CSH, caused by their incompatibility, have decreased. As a result, the rubber particles are more uniformly dispersed among the CSH particles, leading to more stable bonds between them. Figure 4.4 also illustrates the interfaces between CSH/CMC and RH/CMC from a close-up view, highlighting the deep embedding of CMC within both the CSH and RH components of the composite.

To assess the orientational order of RH in CSH/RH and CSH/RH/CMC composites, the s-order parameter was calculated. The s-order parameter for rubber in both

Figure 4.4: *z-density of CSH/RH/CMC composite.*

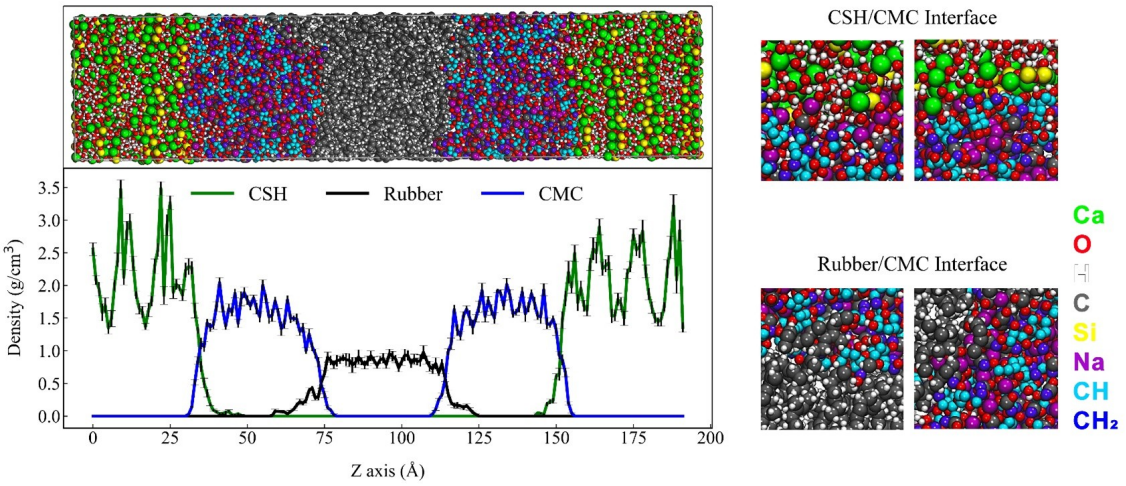

CSH/RH and CSH/RH/CMC systems was analyzed over a 1 ns NVT molecular dynamics simulation (Figure 4.5). The results show that the s-order parameter remains consistent in both systems, with fluctuations around an average value of approximately 0.33. This suggests that the addition of the CMC polymer does not significantly influence the orientational order of the rubber molecules.

Figure 4.5: *S-order parameter variations for RH system in both CSH/RH and CSH/RH/CMC composites.*

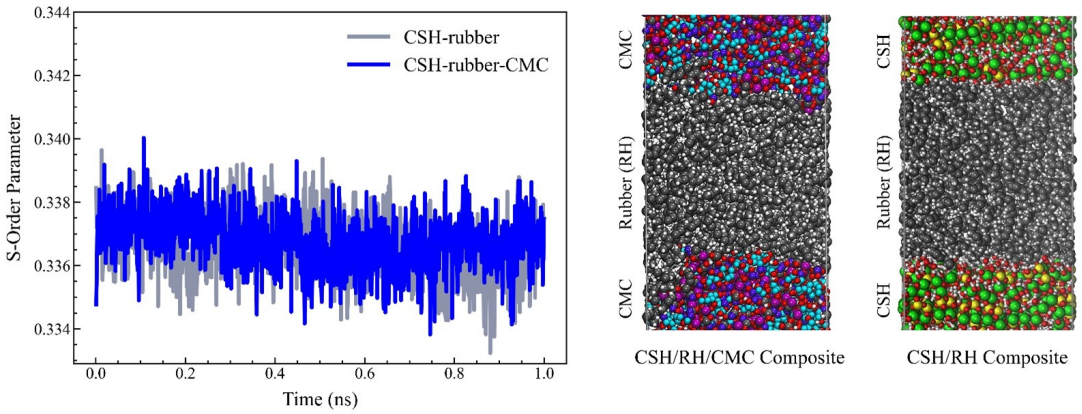

To investigate the effect of temperature variations on the adhesion energy of composites, equilibrium simulations were performed in the NVT ensemble at five different

temperatures: 280 K, 290 K, 300 K, 310 K, and 320 K. Subsequently, the change in entropy (ΔS) for both systems was calculated by plotting $\Delta E/T$ against $1/T$ (Figure 4.6). As shown in Figure 4.6 and Table 4.1, the change in entropy with temperature variations was found to be higher for the CSH/RH/PVOH composite, indicating that the adhesion of PVOH to the CSH matrix is more entropic in nature. This suggests that the adhesion property of PVOH may decrease with temperature changes. In contrast, the lower entropy change observed in the CSH/RH/CMC composite implies that its adhesion property is less affected by temperature variations, making it more stable under changing thermal conditions.

Table 4.1: *Energetic and entropic values of total adhesion energy for CSH/RH/PVOH and CSH/RH/CMC composites.*

Structure	ΔE (kcal/mol), 300 K	ΔS (kcal/mol K)
CMC-Composite	-5337.85	6.10
PVOH-Composite	-4559.24	12.58

Figure 4.6: *Comparison of adhesion energy changes with temperature variation for CSH/RH/CMC and CSH/RH/PVOH composite systems.*

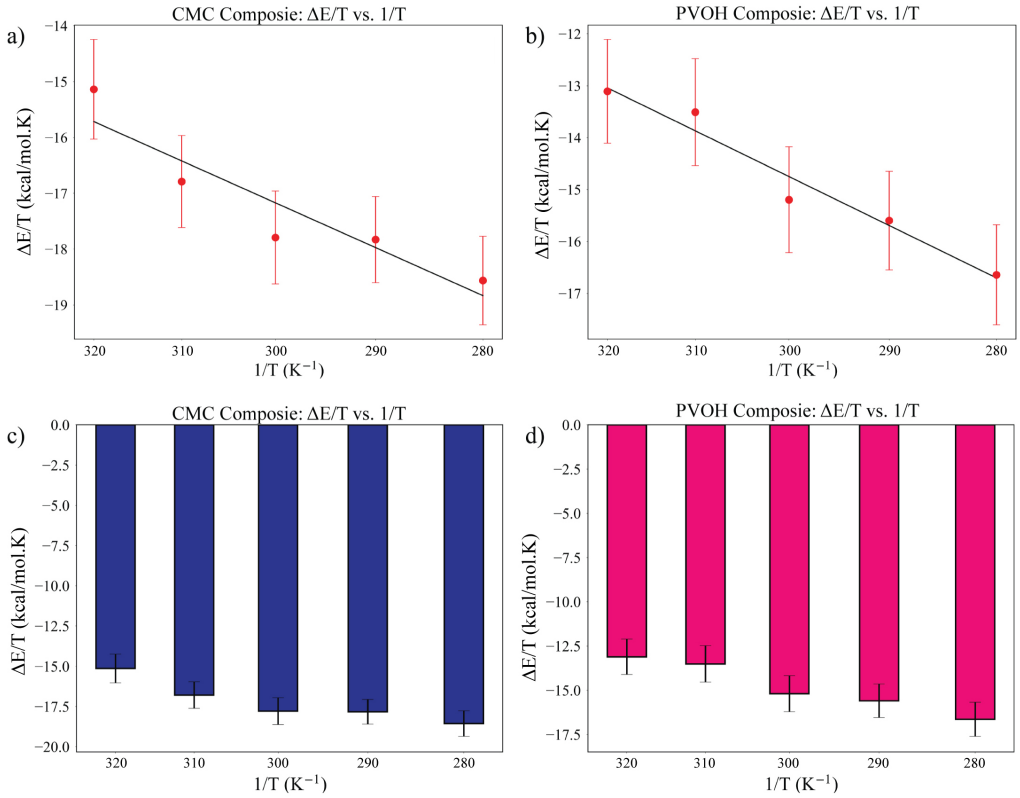

4.4 CSH/RH/Carbon Chain Composite

Figure 4.7 shows the effect of adding SiO_2 and OH-functionalized carbon chains at the interface between CSH and RH. We first calculated the interfacial adhesion energy of the CSH/RH/SiO_2 and CSH/RH/OH composites. As explained in Eq. (3.32), the adhesion energy is obtained by subtracting the sum of the total energies of the individual components from the total energy of the composite. The CSH/RH/SiO_2 system showed an increase of 16.62% in interfacial adhesion energy compared to the CSH/RH/OH composite, indicating stronger bonding and a more compatible structure. To understand this

result, we examined the atomic interactions in the interface using RDF plots. As Figure 4.7 shows, the oxygen atoms in SiO_2 interact stronger with Ca^{2+} ions in CSH than the oxygen atoms in the OH groups. This outcome likely happens because SiO_2 contains more oxygen atoms than OH, giving it more chances to bond with CSH.

Figure 4.7: *(a) Comparison of total adhesion energy between CSH/RH/SiO_2 and CSH/RH/OH systems; (b) Comparing RDF plots of CSH/RH/SiO_2 and CSH/RH/OH systems.*

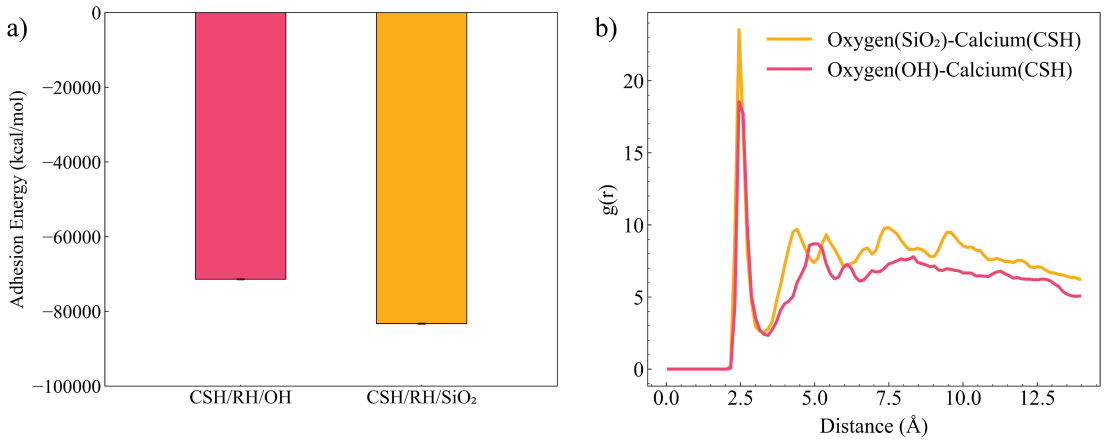

4.5 ZIF-8/PIM-1-based MMMs

Before analyzing the gas permeation properties, we first assessed the density distribution of the ZIF-8/PIM-1 MMMs along the membrane z-axis. As described before, the 21-step compaction procedure [154] was used to create the atomistic models of MMMs. Because of the temperatures and pressures used in the 21-step MD simulations, it is essential to check the reliability of the final MMM model. A uniform density profile is necessary to confirm that the packing process does not cause artificial densification or voids in the polymer phase. As illustrated in Figure 4.8, the density of the PIM-1 matrix remains constant at $1.05 \pm 0.02\ \mathrm{g\,cm^{-3}}$, in close agreement with values reported in the literature [165]. Throughout the slab, the bulk density of the polymer is unaffected by the

presence of ZIF-8 particles. As a result, the inherent mechanical characteristics, and consequently, the interfacial morphology relevant to gas transport of PIM-1 are maintained for all remaining analyses.

Figure 4.8: *Density analysis along the z-axis for: (a) cryZIF-8/PurePIM-1, (b) cryZIF-8/PurePIM-1 MMM's interfacial zone, (c) aZIF-8@0.4GPa/PurePIM-1, and (d) aZIF-8@0.4GPa/PurePIM-1 MMM's interfacial zone.*

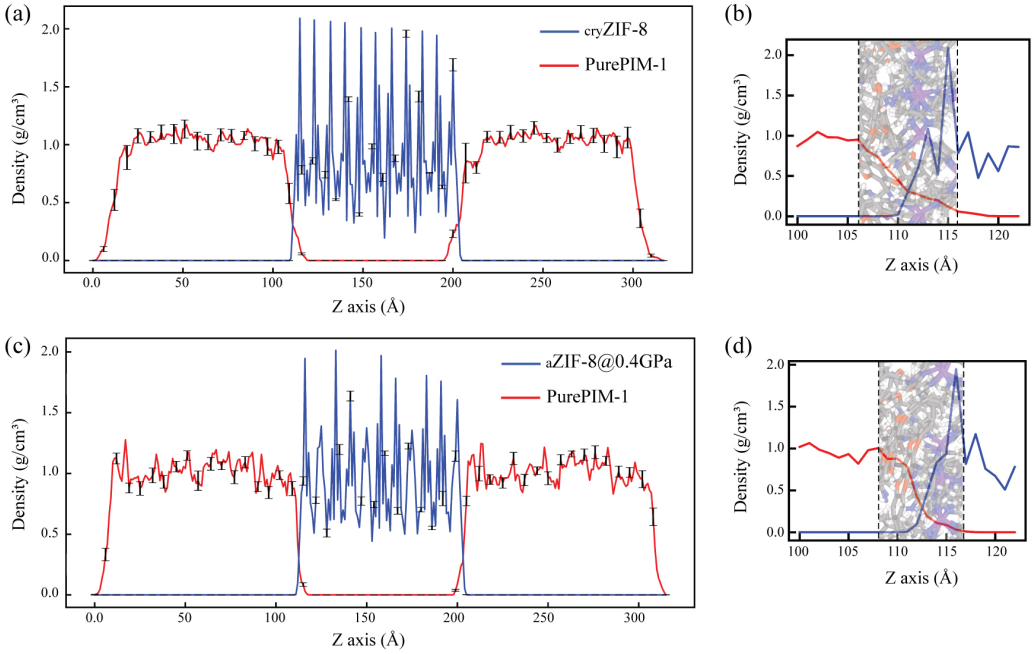

To compare the compatibility between ZIF-8 and PIM-1 in their respective composites, we calculated the interfacial adhesion energy using Eq. (3.33). For each system, the total energies of the isolated components were subtracted from the total energy of the corresponding MMMs. This procedure was applied to the cryZIF-8/PurePIM-1, aZIF-8@0.4 GPa/PurePIM-1, cryZIF-8/AF-PIM-1, and aZIF-8@0.4 GPa/AF-PIM-1 composites, as illustrated in Figure 4.10. Both of the MMM structures that contain aZIF-8@0.4 structure, the aZIF-8@0.4 GPa/PurePIM-1 and aZIF-8@0.4 GPa/AF-PIM-1 MMMs exhibited higher adhesion, indicating that amorphization of ZIF-8 enhances its compatibility with PIM-1 and therefore improves its industrial applicability.

RDF analyses were performed to probe atomic interactions at the ZIF-8/PIM-1 interface in all four MMMs. Pronounced peaks corresponding to N$\cdots$H contacts, between the nitrogen atoms of PIM-1 and the hydrogen atoms of ZIF-8, appeared in RDF plots. These peaks were notably higher for composites containing pristine PIM-1, revealing stronger N$\cdots$H interactions in both crystalline and amorphous ZIF-8 systems. The difference arises from the bonding environments of the nitrogen atoms. In pristine PIM-1 each nitrogen belongs to a nitrile group (C$\equiv$N) and is therefore only triple-bonded to carbon, leaving its lone pair available for intermolecular interactions. In AF-PIM-1, however, each nitrogen forms one C–N single bond and two N–H single bonds (NH_2). This saturated, lower-energy configuration restricts the lone pair and reduces both the driving force and the freedom for interacting with neighbouring atoms, leading to weaker N$\cdots$H contacts with ZIF-8 (Figure 4.9).

Figure 4.9: *Atomistic structures of (a) AF-PIM-1 and (b) PIM-1 monomers.*

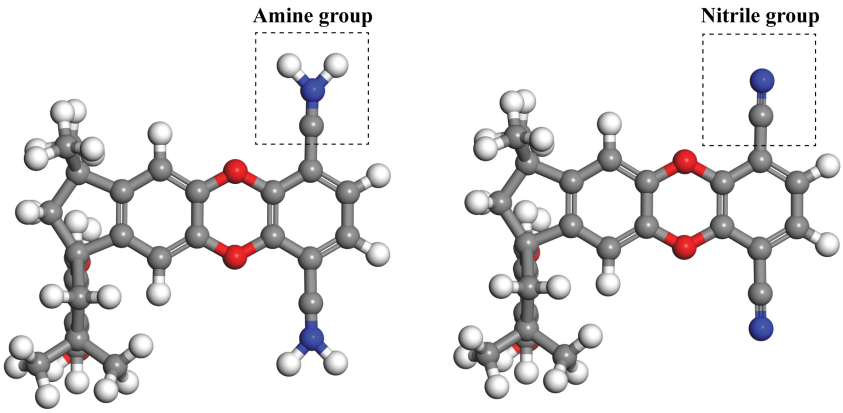

Figure 4.10: *(a) Adhesion energy analysis for ZIF-8/PIM-1 MMMs, (b) RDFs analysis for the hydrogen atoms of surface imidazolate of the ZIF-8 (both cryZIF-8 and aZIF-8@0.4GPa) and the nitrogen atoms of PIM-1 (pure PIM-1 and AF-PIM-1), (c) the representation of nitrogen atoms of pure PIM-1 and AF-PIM-1 in interaction with hydrogen atoms of surface imidazolate of the ZIF-8 (The interacting atoms have been highlighted in yellow).*

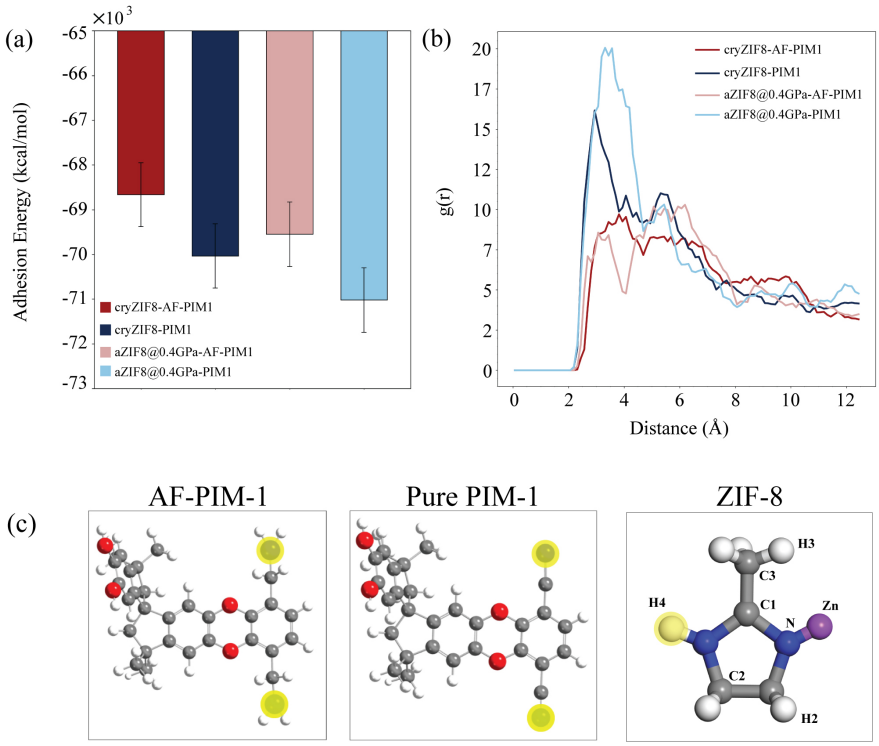

According to the RDF results shown in Figure 4.10, we initially observed higher interaction between the hydrogen atoms of ZIF-8 and the nitrogen atoms of PIM-1 rather than other interfacial interactions between two structures. However, this observation may be misleading. During the membrane construction process, hydrogen atoms were added to terminate the surface nitrogen atoms of ZIF-8. As a result, the surface of ZIF-8 contains an artificially high number of hydrogen atoms, which increases the apparent interaction

with nitrogen atoms in RDF plots. These additional hydrogen atoms are not part of the original ZIF-8 structure and do not represent actual interfacial bonding. Therefore, they can mislead the interpretation of interfacial interactions between ZIF-8 and PIM-1. This is an important issue to consider when using MD simulations to analyze interfacial interactions through RDF in MMMs. To avoid this issue, we focused on more meaningful atom pairs:(a) the interaction between zinc atoms of ZIF-8 and nitrogen atoms of PIM-1, and (b) the interaction between nitrogen atoms of ZIF-8 and oxygen atoms of PIM-1.

In Figure 4.11a, the RDF curves show that the Zn–N interaction was stronger in the ZIF-8/PIM1 system compared to the ZIF-8/AF-PIM1 system. This indicates that pure PIM-1 interacts more strongly with ZIF-8 than AF-PIM-1. One possible reason is that the lone pairs of electrons on the nitrogen atoms in pure PIM-1 are more available for interaction, whereas in AF-PIM-1, their availability is partially restricted due to the hydrogen atoms bonded to the nitrogen atoms. Furthermore, Figure 4.11b presents the RDF profiles for the interaction between nitrogen atoms of ZIF-8 and oxygen atoms of PIM-1 and AF-PIM-1. The RDF curves across all four systems (crystalline/aZIF-8@0.4GPa with pure/AF PIM-1) are similar to eachother. This indicates that the oxygen atoms in both types of PIM-1 occupy similar spatial positions and have similar interaction tendencies with the nitrogen atoms of ZIF-8. Therefore, the presence of amine functional groups in AF-PIM-1 does not significantly affect this particular interaction. Finally, Figure 4.11c provides atomic-level visualizations of the interacting atoms. The atoms involved in the RDF analysis are highlighted in yellow, supporting the interpretation of the RDF plots.

Figure 4.11: *RDF analysis between ZIF-8 and PIM-1 structures: (a) zinc atoms of ZIF-8 and nitrogen atoms of PIM-1, (b) nitrogen atoms of surface imidazlate of the ZIF-8 and oxygen atoms of PIM-1. For the ZIF-8 structure, both cryZIF-8 and aZIF-8@0.4GPa structures are included; for PIM-1, both pure PIM-1 and AF-PIM-1 structures are considered. (c) Atomic representation of the interacting sites between ZIF-8 and PIM-1, with the interacting atoms highlighted in yellow.*

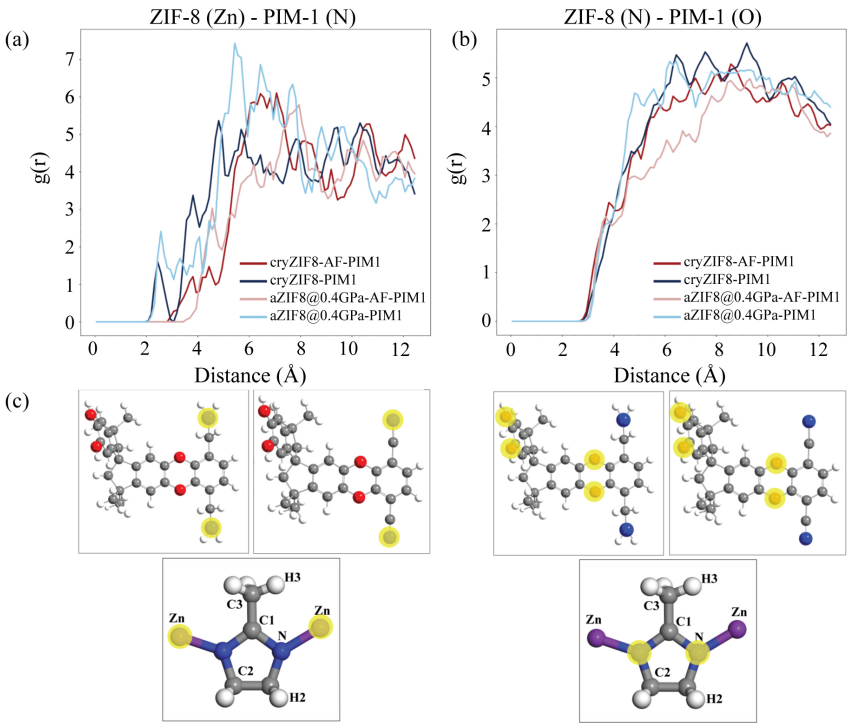

In Section 3.3, we show how the Maxwell and modified Felske models predict gas transport through MMMs by integrating the permeability data of the separate polymer and filler phases. The Maxwell model is generally used when the volume fraction of filler particles (ZIF-8 in this study) is less than 0.2. At higher values of ϕ there are deviations between the experimental permeability of MMM and the permeability that Maxwell model predicts. Specially in higher values of ϕ ($\phi \rightarrow \phi_m$, ϕ_m: maximum packing volume

fraction of filler particles), the Maxwell fails to predict the gas permeability correctly. Another limitation of the Maxwell model is that it fails to account for particle size distribution, particle shape, and particle aggregation [174]. Several prediction models have been suggested to overcome the limitations of the Maxwell model. One of these models is called the modified-Felske model [174]. As it is described in Section 3.3, this model considers the effect of morphology and volume fraction of filler particles.

In this part, we have compared the accuracy of Maxwell and modified-Felske models in predicting the permeability of CO_2 through cryZIF-8/PIM-1 and aZIF-8@0.4 GPa/-PIM-1 MMMs. In our calculations, the volume fraction of ZIF-8 was set to 0.28 to be consistent with the experimental data [175]. We adapted the *li* (the ZIF-8/PIM-1 interfacial region length) of both MMMs from the z-density analysis of MD results as shown in Figure 4.8. The *li* parameters for cryZIF-8/PIM-1 and aZIF-8@0.4 GPa/PIM-1 MMMs were 15 and 11 Å, respectively. The permeability of CO_2 through aZIF-8@0.4 and cryZIF-8 was calculated using GCMC [162] and EMD simulations and the permeability values for PIM-1 were adopted from previously reported literature data [176]. As it is shown in Figure 4.12, predicting permeability of MMM using modified Felske models results in smaller deviation from experimental data rather than Maxwell model. Experimental data in Figure 4.12 is taken from Bushell et al. [175] This is due to including both *li* and ϕ_m in modified Felske model. The permeability in all parts of the polymer phase is not uniform, and the permeability of interfacial regions is given by $P_i = \frac{P_c}{A}$, where A, called the chain immobilization factor, is an empirical constant used to tell the difference between the permeability of the interfacial polymer layer and that of the bulk polymer matrix. In practice, A is often taken to be between 3 and 4 [144]. Throughout our calculations, we assume A = 3. However, because the Maxwell model assumes ideal mixing in MMMs and ignores interfacial voids, it tends to give larger errors compared to experimental data.

Figure 4.12: *Comparison of permeability predictions by the Maxwell and modified Felske models for MMMs.*

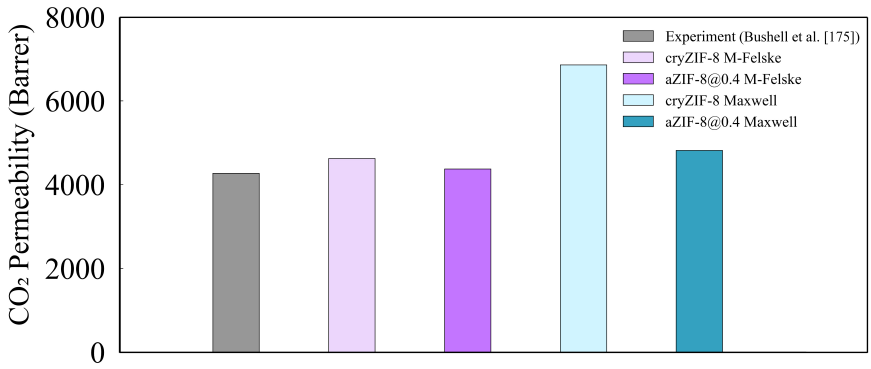

Table 4.2: *Comparison of PLD, the LCD, and density for ZIF-8.*

Material Name	**PLD (Å)**	**LCD (Å)**	**Density (g/cm^3)**
cryZIF-8	3.425	11.508	0.925
aZIF-8@0.4GPa	3.177	10.899	0.980

We investigated how pressure affects ZIF-8 performance while mimicking industrial gas-separation conditions. Because, MOFs and ZIFs used in industry usually contain defects rather than being perfect crystals. As shown in Table 4.2, both the pore limiting diameter (PLD) and the largest cavity diameter (LCD) of ZIF-8 reduces under pressure while its density increases [162]. As shown in Figure 4.12, MMMs containing aZIF-8@0.4GPa exhibit permeabilities that agree more closely with experimental values than those with crystalline ZIF-8 when evaluated using both the Maxwell and modified Felske models. Overall, this work highlights the importance of studying different forms of ZIF-8 for MMM applications.

5. CONCLUSION

In this thesis, we focus on understanding the interfacial interactions of composites, a key challenge in materials design. The compatibility between composite layers critically influences properties such as stability, durability, and workability. This thesis examines two classes of composites: cementitious composites and ZIF-8/PIM-1 MMMs.

For cementitious composites, we performed MD simulations on a CSH/RH sandwich-like composite. Due to the hydrophilic nature of CSH and the hydrophobicity of RH, voids form at the interface, reducing the composite's mechanical strength. To address this, we evaluated polymers, including PCE, CMC, PVOH, and functionalized carbon chains with (OH) and (SiO_2) as potential interfacial bridges. Our results showed that inserting PCE between CSH and RH increased the adhesion energy by 7.3% compared to the untreated CSH/RH composite. RDF analysis further confirmed pairwise interactions between PCE's oxygen atoms and CSH's Ca^{2+} ions, indicating enhanced interfacial compatibility.

We also compared the performance of CMC and PVOH as interfacial polymers. PVOH, a non-biodegradable polymer, is conventionally used in CSH/RH composites. In contrast, CMC, a cellulose derivative, is a prominent industrial biopolymer. We compared the binding performance of these two polymers by incorporating them into the CSH/RH matrix. CMC improved the matrix compatibility more effectively, increasing the adhesion energy of the CSH/RH/CMC system by 17.08% compared to CSH/RH/PVOH. Additionally, RDF analysis revealed stronger pairwise interactions between CMC and CSH than between PVOH and CSH.

Finally, our analysis of carbon chains as an interfacial layer between CSH and RH revealed that SiO_2-functionalized carbon chains exhibited superior performance in bridging the hydrophilic and hydrophobic phases. The interfacial adhesion energy of the

CSH/RH/SiO_2 system increased by 16.63% compared to the untreated composite. Furthermore, RDF analysis supported these findings, demonstrating stronger pairwise interactions between SiO_2 and CSH.

In the ZIF-8/PIM-1 system, we investigated four MMMs: crystalline ZIF-8 with pure PIM-1, crystalline ZIF-8 with AF-PIM-1, pressurized ZIF-8@0.4 GPa with pure PIM-1, and pressurized ZIF-8@0.4 GPa with AF-PIM-1. The MMMs incorporating pressurized ZIF-8 structures exhibited a 1.4% higher interfacial adhesion energy compared to those with crystalline ZIF-8. RDF analysis revealed that MMMs containing pure PIM-1 demonstrate stronger interfacial interactions than those with AF-PIM-1. Additionally, permeability predictions using the modified Felske model showed closer agreement with experimental values compared to the Maxwell model. Our key contributions to the literature include:

- We systematically evaluated five interface polymer candidates, PCE, CMC, PVOH, and carbon chains functionalized with OH- and silica (SiO_2) groups for their effectiveness as bridging agents at rubber-concrete interfaces.
- We computed RDFs, z-density profiles, and interfacial adhesion energies for the interface polymers between RH and CSH.
- We appplied continuum modelling to predict gas permeability in MMMs composed of crystalline ZIF-8 and ZIF-8 structures produced under a pressure of 0.4 GPa.
- We compared the performance of MMMs composed of PIM-1 and amine-functionalized PIM-1 with ZIF-8 structures.

It is important to highlight the assumptions we made in this thesis. We first assumed that CSH is a representative phase of concrete. Although CSH is the primary

hydration product responsible for the mechanical strength and structural integrity of concrete, other hydration products, such as calcium hydroxide (portlandite, $Ca(OH)_2$), tricalcium aluminate (C_3A), and tetracalcium aluminoferrite (C_4AF), also coexist within concrete and may influence its overall properties and behavior.

In the ZIF-8/PIM-1 MMMs, we used the modified Felske model to predict permeability and compared our results with only a single experimental data. Ideally, various experimental data should be considered to comprehensively validate our simulation results. Additionally, using interface-specific force fields in both rubber/concrete and ZIF-8/PIM-1 composites, which account for the surface chemistry of the components, would further enhance the validity and reliability of our simulation results.

As a future work, we propose employing machine learning techniques to systematically evaluate diverse material structures, which could enhance predictive modelling and advance fundamental understanding in materials design. Various amorphous structures of ZIF-8 (taken from different pressure regimes) can be used in the MMM models to figure out their potential in gas separation applications. Furthermore, non-equilibrium MD simulations can be designed to predict a more realistic gas separation mechanism in composites.

Overall, the results obtained in this thesis will provide both fundamental insights and practical methodologies for future model development in composite systems.

REFERENCES

[1] D. Gay, *Composite materials: design and applications*. CRC press, 2022.

[2] D. K. Rajak, D. D. Pagar, R. Kumar, and C. I. Pruncu, "Recent progress of reinforcement materials: a comprehensive overview of composite materials," *Journal of Materials Research and Technology*, vol. 8, no. 6, pp. 6354–6374, 2019.

[3] D. Hale, "The physical properties of composite materials," *Journal of Materials Science*, vol. 11, no. 11, pp. 2105–2141, 1976.

[4] R. M. Jones, *Mechanics of composite materials*. CRC press, 2018.

[5] I. Oladele, N. L. Onuh, S. Siengchin, S. M R, and S. Adelani, "Modern applications of polymer composites in structural industries: A review of philosophies, product development, and graphical applications," *Applied Science and Engineering Progress*, vol. 17, p. 6884, 01 2024.

[6] M. A. Kashfipour, N. Mehra, and J. Zhu, "A review on the role of interface in mechanical, thermal, and electrical properties of polymer composites," *Advanced Composites and Hybrid Materials*, vol. 1, no. 3, pp. 415–439, 2018.

[7] I. O. Oladele, T. F. Omotosho, and A. A. Adediran, "Polymer-based composites: an indispensable material for present and future applications," *International Journal of Polymer Science*, vol. 2020, no. 1, p. 8834518, 2020.

[8] M. M. Zagho, E. A. Hussein, and A. A. Elzatahry, "Recent overviews in functional polymer composites for biomedical applications," *Polymers*, vol. 10, no. 7, 2018.

[9] D. Hou, *Molecular simulation on cement-based materials*, vol. 10. Springer, 2020.

[10] H. M. Jennings, "Refinements to colloid model of C–S–H in cement: CM-II," *Cement and Concrete Research*, vol. 38, no. 3, pp. 275–289, 2008.

[11] P. K. Mehta and P. J. Monteiro, *Concrete microstructure, properties, and materials*. McGraw-hill, 2006.

[12] Y. Zhou, C. A. Orozco, E. Duque-Redondo, H. Manzano, G. Geng, P. Feng, P. J. Monteiro, and C. Miao, "Modification of poly (ethylene glycol) on the microstructure and mechanical properties of calcium silicate hydrates," *Cement and Concrete Research*, vol. 115, pp. 20–30, 2019.

[13] Y. Zhou, L. Tang, J. Liu, and C. Miao, "Interaction mechanisms between organic and inorganic phases in calcium silicate hydrates/poly (vinyl alcohol) composites," *Cement and Concrete Research*, vol. 125, p. 105891, 2019.

[14] D. Hou, Z. Lu, X. Li, H. Ma, and Z. Li, "Reactive molecular dynamics and experimental study of graphene-cement composites: Structure, dynamics and reinforcement mechanisms," *Carbon*, vol. 115, pp. 188–208, 2017.

[15] M. S. Konsta-Gdoutos, Z. S. Metaxa, and S. P. Shah, "Highly dispersed carbon nanotube reinforced cement based materials," *Cement and Concrete Research*, vol. 40, no. 7, pp. 1052–1059, 2010.

[16] Y. Zhou, H. Zheng, Y. Qiu, X. Zou, and J. Huang, "A molecular dynamics study on the structure, interfaces, mechanical properties, and mechanisms of a calcium silicate hydrate/2D-silica nanocomposite," *Frontiers in Materials*, vol. 7, p. 127, 2020.

[17] Q. Han, Y. Yang, J. Zhang, J. Yu, D. Hou, B. Dong, and H. Ma, "Insights into the interfacial strengthening mechanism of waste rubber/cement paste using polyvinyl alcohol: Experimental and molecular dynamics study," *Cement and Concrete Composites*, vol. 114, p. 103791, 2020.

[18] M. M. Reda Taha, A. S. El-Dieb, M. Abd El-Wahab, and M. Abdel-Hameed, "Mechanical, fracture, and microstructural investigations of rubber concrete," *Journal of Materials in Civil Engineering*, vol. 20, no. 10, pp. 640–649, 2008.

[19] N. Segre and I. Joekes, "Use of tire rubber particles as addition to cement paste," *Cement and Concrete Research*, vol. 30, no. 9, pp. 1421–1425, 2000.

[20] L. He, Y. Ma, Q. Liu, and Y. Mu, "Surface modification of crumb rubber and its influence on the mechanical properties of rubber-cement concrete," *Construction and Building Materials*, vol. 120, pp. 403–407, 2016.

[21] B. Muñoz-Sánchez, M. J. Arévalo-Caballero, and M. C. Pacheco-Menor, "Influence of acetic acid and calcium hydroxide treatments of rubber waste on the properties of rubberized mortars," *Materials and Structures*, vol. 50, no. 1, p. 75, 2017.

[22] Q. Dong, B. Huang, and X. Shu, "Rubber modified concrete improved by chemically active coating and silane coupling agent," *Construction and Building Materials*, vol. 48, pp. 116–123, 2013.

[23] L. Ferrari, L. Bernard, F. Deschner, J. Kaufmann, F. Winnefeld, and J. Plank, "Characterization of polycarboxylate-ether based superplasticizer on cement clinker surfaces," *Journal of the American Ceramic Society*, vol. 95, no. 7, pp. 2189–2195, 2012.

[24] M. S. Rahman, M. S. Hasan, A. S. Nitai, S. Nam, A. K. Karmakar, M. S. Ahsan, M. J. A. Shiddiky, and M. B. Ahmed, "Recent developments of carboxymethyl cellulose," *Polymers*, vol. 13, no. 8, 2021.

[25] J. Yu, H. Zheng, D. Hou, J. Zhang, and W. Xu, "Silane coupling agent modification treatment to improve the properties of rubber–cement composites," *ACS Sustainable Chemistry & Engineering*, vol. 9, no. 38, pp. 12899–12911, 2021.

[26] W. Xie, T. Li, A. Tiraferri, E. Drioli, A. Figoli, J. C. Crittenden, and B. Liu, "Toward the next generation of sustainable membranes from green chemistry principles," *ACS Sustainable Chemistry & Engineering*, vol. 9, no. 1, pp. 50–75, 2020.

[27] S. Karki, G. Hazarika, D. Yadav, and P. G. Ingole, "Polymeric membranes for industrial applications: Recent progress, challenges and perspectives," *Desalination*, vol. 573, p. 117200, 2024.

[28] B. Comesaña-Gándara, J. Chen, C. G. Bezzu, M. Carta, I. Rose, M.-C. Ferrari, E. Esposito, A. Fuoco, J. C. Jansen, and N. B. McKeown, "Redefining the Robeson upper bounds for CO_2/CH_4 and CO_2/N_2 separations using a series of ultrapermeable benzotriptycene-based polymers of intrinsic microporosity," *Energy & Environmental Science*, vol. 12, no. 9, pp. 2733–2740, 2019.

[29] A. Mollahosseini, M. N. Dafchahi, S. K. Salestan, J. W. Chew, M. Mozafari, M. Soroush, S. Hrapovic, U. D. Hemraz, R. Giro, M. B. Steiner, *et al.*, "Polymeric membranes in carbon capture, utilization, and storage: current trends and future directions in decarbonization of industrial flue gas and climate change mitigation," *Energy & Environmental Science*, vol. 18, no. 11, pp. 5025–5092, 2025.

[30] L. M. Robeson, "The upper bound revisited," *Journal of Membrane Science*, vol. 320, no. 1-2, pp. 390–400, 2008.

[31] Y. Zhang, B. H. Yin, L. Huang, L. Ding, S. Lei, S. G. Telfer, J. Caro, and H. Wang, "MOF membranes for gas separations," *Progress in Materials Science*, vol. 151, p. 101432, 2025.

[32] Q. Ma, J. Li, Y. Li, and J. Choi, "Recent progress and issues facing zeolite and metal-organic framework membranes: From membrane synthesis to applications," *Journal of Membrane Science*, vol. 690, p. 122201, 2024.

[33] M. Zhao, Y. Yang, and X.-S. Gu, "MOF based CO_2 capture: Adsorption and membrane separation," *Inorganic Chemistry Communications*, vol. 152, p. 110722, 2023.

[34] M. Usman, N. Iqbal, T. Noor, N. Zaman, A. Asghar, M. M. Abdelnaby, A. Galadima, and A. Helal, "Advanced strategies in metal-organic frameworks for CO_2 capture and separation," *The Chemical Record*, vol. 22, no. 7, p. e202100230, 2022.

[35] G. M. Monsalve-Bravo, R. C. Dutta, and S. K. Bhatia, "Multiscale simulation of gas transport in mixed-matrix membranes with interfacial polymer rigidification," *Microporous and Mesoporous Materials*, vol. 296, p. 109982, 2020.

[36] J. C. Maxwell, *A treatise on electricity and magnetism*, vol. 1. Clarendon press, 1873.

[37] R. Pal, "Permeation models for mixed matrix membranes," *Journal of colloid and interface science*, vol. 317, no. 1, pp. 191–198, 2008.

[38] S. S. Pendhari, T. Kant, and Y. M. Desai, "Application of polymer composites in civil construction: A general review," *Composite Structures*, vol. 84, no. 2, pp. 114–124, 2008.

[39] L. Barcelo, J. Kline, G. Walenta, and E. Gartner, "Cement and carbon emissions," *Materials and Structures*, vol. 47, 06 2014.

[40] E. Gartner and H. Hirao, "A review of alternative approaches to the reduction of CO_2 emissions associated with the manufacture of the binder phase in concrete," *Cement and Concrete Research*, vol. 78, pp. 126–142, 2015. Keynote papers from 14th International Congress on the Chemistry of Cement (ICCC 2015).

[41] F. Lollini, E. Redaelli, and L. Bertolini, "A study on the applicability of the efficiency factor of supplementary cementitious materials to durability properties," *Construction and Building Materials*, vol. 120, pp. 284–292, 2016.

[42] P. Monteiro and P. Mehta, *Concrete: Microstructure, Properties and Materials*. McGraw-Hill, 06 2006.

[43] B. Persson, "Experimental studies on shrinkage of high-performance concrete," *Cement and Concrete Research*, vol. 28, no. 7, pp. 1023–1036, 1998.

[44] R. Feiz, J. Ammenberg, L. Baas, M. Eklund, A. Helgstrand, and R. Marshall, "Improving the CO_2 performance of cement, part I: utilizing life-cycle assessment and key performance indicators to assess development within the cement industry," *Journal of Cleaner Production*, vol. 98, pp. 272–281, 2015.

[45] A. Neville, "The confused world of sulfate attack on concrete," *Cement and Concrete Research*, vol. 34, no. 8, pp. 1275–1296, 2004.

[46] D. Hobbs and M. Taylor, "Nature of the thaumasite sulfate attack mechanism in field concrete," *Cement and Concrete Research*, vol. 30, no. 4, pp. 529–533, 2000.

[47] Z. Shi, B. Lothenbach, M. R. Geiker, J. Kaufmann, A. Leemann, S. Ferreiro, and J. Skibsted, "Experimental studies and thermodynamic modeling of the carbonation of portland cement, metakaolin and limestone mortars," *Cement and Concrete Research*, vol. 88, pp. 60–72, 2016.

[48] J. Mao, W. Jin, H. Zhang, C. Xu, and J. Xia, "Technology for enhancing durability of structures of sea-sand concrete and its application," *Journal of Chinese Society for Corrosion and Protection*, vol. 35, pp. 563–570, 02 2016.

[49] S. A. Bernal, E. D. Rodríguez, A. P. Kirchheim, and J. L. Provis, "Management and valorisation of wastes through use in producing alkali-activated cement materials," *Journal of Chemical Technology & Biotechnology*, vol. 91, no. 9, pp. 2365–2388, 2016.

[50] B. Bhushan, *Introduction to nanotechnology*. Springer, 2017.

[51] F. Sanchez and K. Sobolev, "Nanotechnology in concrete–a review," *Construction and Building Materials*, vol. 24, no. 11, pp. 2060–2071, 2010.

[52] R. P. Feynman, "There's plenty of room at the bottom," *Journal of Microelectromechanical Systems*, vol. 1, no. 1, pp. 60–66, 1992.

[53] I. G. Richardson, "The calcium silicate hydrates," *Cement and Concrete Research*, vol. 38, no. 2, pp. 137–158, 2008.

[54] M. Mirzahosseini and K. A. Riding, "Influence of different particle sizes on reactivity of finely ground glass as supplementary cementitious material (SCM)," *Cement and Concrete Composites*, vol. 56, pp. 95–105, 2015.

[55] A. Allen, J. Thomas, and H. Jennings, "Composition and density of nanoscale calcium–silicate–hydrate in cement," *Nature Materials*, vol. 6, pp. 311–6, 05 2007.

[56] R. Alyousef, W. Ahmad, A. Ahmad, F. Aslam, P. Joyklad, and H. Alabduljabbar, "Potential use of recycled plastic and rubber aggregate in cementitious materials for sustainable construction: A review," *Journal of Cleaner Production*, vol. 329, p. 129736, 2021.

[57] S. Karunarathna, S. Linforth, A. Kashani, X. Liu, and T. Ngo, "Effect of recycled rubber aggregate size on fracture and other mechanical properties of structural concrete," *Journal of Cleaner Production*, vol. 314, p. 128230, 2021.

[58] A. Mohajerani, L. Burnett, J. Smith, S. Markovski, G. Rodwell, M. T. Rahman, H. Kurmus, M. Mirzababaei, A. Arulrajah, and F. Maghool, "Recycling waste rubber tyres in construction materials and associated environmental considerations: A review," *Resources Conservation and Recycling*, vol. 155, 01 2020.

[59] M. Valente and A. Sibai, "Rubber/crete: Mechanical properties of scrap to reuse tire-derived rubber in concrete; a review," *SAGE Open*, vol. 17, p. 8, 06 2019.

[60] J. Mei, G. Xu, W. Ahmad, K. Khan, M. N. Amin, F. Aslam, and A. Alaskar, "Promoting sustainable materials using recycled rubber in concrete: A review," *Journal of Cleaner Production*, vol. 373, p. 133927, 2022.

[61] S. Kaza, L. Yao, P. Bhada-Tata, and F. Van Woerden, *What a waste 2.0: a global snapshot of solid waste management to 2050*. World Bank Publications, 2018.

[62] R. Roychand, R. J. Gravina, Y. Zhuge, X. Ma, O. Youssf, and J. E. Mills, "A comprehensive review on the mechanical properties of waste tire rubber concrete," *Construction and Building Materials*, vol. 237, p. 117651, 2020.

[63] Y. Feng, Q. Wang, L. Li, Y. Ma, and X. Li, "Multiscale analysis of silane coupling agent modified rubber-fiber concrete interfaces," *Materials Today Communications*, vol. 35, p. 105960, 04 2023.

[64] Z. Chen, L. Li, and Z. Xiong, "Investigation on the interfacial behaviour between the rubber-cement matrix of the rubberized concrete," *Journal of Cleaner Production*, vol. 209, pp. 1354–1364, 12 2018.

[65] I. Glushankova, A. Ketov, M. Krasnovskikh, L. Rudakova, and I. Vaisman, "End of life tires as a possible source of toxic substances emission in the process of combustion," *Resources*, vol. 8, p. 113, 06 2019.

[66] Z. Kerekes, É. Lublóy, and K. Kopecskó, "Behaviour of tyres in fire: Determination of burning characteristics of tyres," *Journal of Thermal Analysis and Calorimetry*, vol. 133, 01 2018.

[67] B. S. Thomas, R. C. Gupta, P. Kalla, and L. Cseteneyi, "Strength, abrasion and permeation characteristics of cement concrete containing discarded rubber fine aggregates," *Construction and Building Materials*, vol. 59, pp. 204–212, 2014.

[68] R. Gupta, "Long term behaviour of cement concrete containing discarded tire rubber," *Journal of Cleaner Production*, vol. 102, 05 2015.

[69] L. He, H. Cai, Y. Huang, Y. Ma, W. Van Den Bergh, L. Gaspar, J. Valentin, Y. E. Vasiliev, K. J. Kowalski, and J. Zhang, "Research on the properties of rubber concrete containing surface-modified rubber powders," *Journal of Building Engineering*, vol. 35, p. 101991, 2021.

[70] W. Huang, X. Huang, Q. Xing, and Z. Zhou, "Strength reduction factor of crumb rubber as fine aggregate replacement in concrete," *Journal of Building Engineering*, vol. 32, p. 101346, 2020.

[71] B. S. Thomas and R. C. Gupta, "A comprehensive review on the applications of waste tire rubber in cement concrete," *Renewable and Sustainable Energy Reviews*, vol. 54, pp. 1323–1333, 2016.

[72] V. Vázquez, J. Luong, M. Bueno, F. Terán, and S. Paje, "Assessment of an action against environmental noise: Acoustic durability of a pavement surface with crumb rubber," *Science of the Total Environment*, vol. 542, pp. 223–230, 2016.

[73] N. N. Eldin and A. B. Senouci, "Rubber-tire particles as concrete aggregate," *Journal of Materials in Civil engineering*, vol. 5, no. 4, pp. 478–496, 1993.

[74] H. A. Toutanji, "The use of rubber tire particles in concrete to replace mineral aggregates," *Cement and Concrete Composites*, vol. 18, no. 2, pp. 135–139, 1996.

[75] K.-H. Chung and Y.-K. Hong, "Introductory behavior of rubber concrete," *Journal of Applied Polymer Science*, vol. 72, no. 1, pp. 35–40, 1999.

[76] J. Kang, Y. Liu, J. Yuan, C. Chen, L. Wang, and Z. Yu, "Effectiveness of surface treatment on rubber particles towards compressive strength of rubber concrete: A numerical study on rubber-cement interface," *Construction and Building Materials*, vol. 350, p. 128820, 2022.

[77] N. N. Gerges, C. A. Issa, and S. A. Fawaz, "Rubber concrete: Mechanical and dynamical properties," *Case Studies in Construction Materials*, vol. 9, p. e00184, 2018.

[78] L. Zheng, X. S. Huo, and Y. Yuan, "Experimental investigation on dynamic properties of rubberized concrete," *Construction and Building Materials*, vol. 22, no. 5, pp. 939–947, 2008.

[79] F. Valentini and A. Pegoretti, "End-of-life options of tyres. a review," *Advanced Industrial and Engineering Polymer Research*, vol. 5, no. 4, pp. 203–213, 2022.

[80] G. Li, Z. Wang, C. K. Leung, S. Tang, J. Pan, W. Huang, and E. Chen, "Properties of rubberized concrete modified by using silane coupling agent and carboxylated sbr," *Journal of Cleaner Production*, vol. 112, pp. 797–807, 2016.

[81] L. Rivas-Vázquez, R. Suárez-Orduña, J. Hernández-Torres, and E. Aquino-Bolaños, "Effect of the surface treatment of recycled rubber on the mechanical strength of composite concrete/rubber," *Materials and Structures*, vol. 48, pp. 2809–2814, 2015.

[82] H. Zhang, M. Gou, X. Liu, and X. Guan, "Effect of rubber particle modification on properties of rubberized concrete," *Journal of Wuhan University of Technology-Mater. Sci. Ed.*, vol. 29, pp. 763–768, 2014.

[83] Y. Feng, D. Qin, L. Li, Y. Li, C. Wang, and P. Wang, "EVA enhances the interfacial strength of EPS concrete: a molecular dynamics study," *Journal of Experimental Nanoscience*, vol. 16, no. 1, pp. 382–396, 2021.

[84] L. Li, D. Qin, Z. Xu, and Y. Feng, "Study on strengthening mechanism of epoxy resin/rubber concrete interface by molecular dynamics simulation," *Advances in Civil Engineering*, vol. 2022, no. 1, p. 5100758, 2022.

[85] X. Tian, J.-N. Kang, M. Dai, X. Li, Y.-Z. Ji, L.-C. Liu, and Y.-M. Wei, "Unleashing tomorrow's potential: A comprehensive exploration of risks in carbon capture and storage," *Renewable and Sustainable Energy Reviews*, vol. 210, p. 115174, 2025.

[86] M. Steyn, J. Oglesby, G. Turan, A. Zapantis, R. Gebremedhin, A. Zapantis, N. Amer, I. Havercroft, R. Ivory-Moore, M. Steyn, *et al.*, "Global status of CCS 2022," *Global CCS Institute: Sydney, Australia*, 2022.

[87] P. R. Shukla, J. Skea, R. Slade, A. Al Khourdajie, R. van Diemen, D. McCollum, M. Pathak, S. Some, P. Vyas, R. Fradera, *et al.*, *Climate change 2022: Mitigation of climate change*, vol. 10. Cambridge University Press Cambridge, UK, 2022.

[88] W. Cao, H. Xu, X. Zhang, W. Xiang, G. Qi, L. Wan, and B. Gao, "Novel post-treatment of ultrasound assisting with acid washing enhance lignin-based biochar for CO_2 capture: adsorption performance and mechanism," *Chemical Engineering Journal*, vol. 471, p. 144523, 2023.

[89] H. Zentou, M. Aliyu, M. A. Abdalla, O. Y. Abdelaziz, B. Hoque, A. M. Alloush, I. M. Tayeb, K. Patchigolla, and M. M. Abdelnaby, "Advancements and challenges in adsorption-based carbon capture technology: From fundamentals to deployment," *The Chemical Record*, vol. 25, no. 1, p. e202400188, 2025.

[90] R. Sims, R. Schaeffer, F. Creutzig, X. Cruz-Núñez, M. D'Agosto, D. Dimitriu, M. Meza, L. Fulton, S. Kobayashi, O. Lah, A. Mckinnon, P. Newman, M. Ouyang, J. Schauer, D. Sperling, and G. Tiwari, *Transport. In: Climate Change 2014: Mitigation of Climate Change. Contribution of Working Group III to the Fifth Assessment Report of the Intergovernmental Panel on Climate Change*. Cambridge University Press, 09 2014.

[91] Z. Liu, Z. Deng, S. Davis, and P. Ciais, "Monitoring global carbon emissions in 2022," *Nature Reviews Earth & Environment*, vol. 4, no. 4, pp. 205–206, 2023.

[92] X. Zheng, D. Streimikiene, T. Balezentis, A. Mardani, F. Cavallaro, and H. Liao, "A review of greenhouse gas emission profiles, dynamics, and climate change mitigation efforts across the key climate change players," *Journal of Cleaner Production*, vol. 234, pp. 1113–1133, 2019.

[93] A. Olabi, T. Wilberforce, K. Elsaid, E. T. Sayed, H. M. Maghrabie, and M. A. Abdelkareem, "Large scale application of carbon capture to process industries–a review," *Journal of Cleaner Production*, vol. 362, p. 132300, 2022.

[94] R. Hou, C. Fong, B. D. Freeman, M. R. Hill, and Z. Xie, "Current status and advances in membrane technology for carbon capture," *Separation and Purification Technology*, vol. 300, p. 121863, 2022.

[95] D. Leeson, N. Mac Dowell, N. Shah, C. Petit, and P. S. Fennell, "A techno-economic analysis and systematic review of carbon capture and storage (CCS) applied to the iron and steel, cement, oil refining and pulp and paper industries, as well as other high purity sources," *International Journal of Greenhouse Gas Control*, vol. 61, pp. 71–84, 2017.

[96] A. Katare, S. Kumar, S. Kundu, S. Sharma, L. M. Kundu, and B. Mandal, "Mixed matrix membranes for carbon capture and sequestration: challenges and scope," *ACS Omega*, vol. 8, no. 20, pp. 17511–17522, 2023.

[97] K. Ramasubramanian, H. Verweij, and W. W. Ho, "Membrane processes for carbon capture from coal-fired power plant flue gas: A modeling and cost study," *Journal of Membrane Science*, vol. 421, pp. 299–310, 2012.

[98] N. Hedin, L. Andersson, L. Bergström, and J. Yan, "Adsorbents for the post-combustion capture of CO_2 using rapid temperature swing or vacuum swing adsorption," *Applied Energy*, vol. 104, pp. 418–433, 2013.

[99] A. B. Rao and E. S. Rubin, "A technical, economic, and environmental assessment of amine-based CO_2 capture technology for power plant greenhouse gas control," *Environmental Science & Technology*, vol. 36, no. 20, pp. 4467–4475, 2002.

[100] B. L. Salvi and S. Jindal, "Recent developments and challenges ahead in carbon capture and sequestration technologies," *SN Applied Sciences*, vol. 1, no. 8, p. 885, 2019.

[101] Z. Xie and J. Hou, "Industrialising Metal Organic Frameworks bridging laboratory innovation and future applications," *Industrial & Engineering Chemistry Research*, vol. 64, no. 16, pp. 7941–7955, 2025.

[102] U. Müller, M. Schubert, F. Teich, H. Puetter, K. Schierle-Arndt, and J. Pastré, "Metal–organic frameworks—prospective industrial applications," *Journal of Materials Chemistry*, vol. 16, no. 7, pp. 626–636, 2006.

[103] H. Li, W. Shi, K. Zhao, H. Li, Y. Bing, and P. Cheng, "Enhanced hydrostability in Ni-doped MOF-5," *Inorganic Chemistry*, vol. 51, no. 17, pp. 9200–9207, 2012.

[104] Y. An, X. Lv, W. Jiang, L. Wang, Y. Shi, X. Hang, and H. Pang, "The stability of MOFs in aqueous solutions—research progress and prospects," *Green Chemical Engineering*, vol. 5, no. 2, pp. 187–204, 2024.

[105] J. Hou, X. Hong, S. Zhou, Y. Wei, and H. Wang, "Solvent-free route for metal–organic framework membranes growth aiming for efficient gas separation," *AIChE Journal*, vol. 65, no. 2, pp. 712–722, 2019.

[106] Z. Li, Y. Wang, J. Zhang, S. Cheng, and Y. Sun, "A short review of advances in MOF glass membranes for gas adsorption and separation," *Membranes*, vol. 14, no. 5, p. 99, 2024.

[107] J. M. Tuffnell, C. W. Ashling, J. Hou, S. Li, L. Longley, M. L. R. Gómez, and T. D. Bennett, "Novel metal–organic framework materials: blends, liquids, glasses and crystal–glass composites," *Chemical Communications*, vol. 55, no. 60, pp. 8705–8715, 2019.

[108] Z. Yin, Y.-B. Zhang, H.-B. Yu, and M.-H. Zeng, "How to create MOF glasses and take advantage of emerging opportunities," *Science Bulletin*, vol. 65, no. 17, pp. 1432–1435, 2020.

[109] A. E. Khudozhitkov, N. Ogiwara, M. Donoshita, H. Kobayashi, A. G. Stepanov, D. I. Kolokolov, and H. Kitagawa, "Dynamics of linkers in metal–organic framework glasses," *Journal of the American Chemical Society*, vol. 146, no. 19, pp. 12950–12957, 2024.

[110] H. Mahdavi, J. F. Olorunyomi, N. T. Eden, C. M. Doherty, D. Acharya, S. J. Smith, X. Mulet, and M. R. Hill, "Design and Development of a Self-Supporting ZIF-62 Glass MOF Membrane with Enhanced Molecular Sieving for High H_2 Separation Efficiency," *ACS Omega*, vol. 10, no. 7, pp. 7441–7451, 2025.

[111] L. M. Robeson, Q. Liu, B. D. Freeman, and D. R. Paul, "Comparison of transport properties of rubbery and glassy polymers and the relevance to the upper bound relationship," *Journal of Membrane Science*, vol. 476, pp. 421–431, 2015.

[112] Q. Ma, H. Jin, and Y. Li, "Tuning the adsorption selectivity of ZIF-8 by amorphization," *Chemistry–A European Journal*, vol. 26, no. 58, pp. 13137–13141, 2020.

[113] S. H. Goh, H. S. Lau, and W. F. Yong, "Metal–organic frameworks (MOFs)-based mixed matrix membranes (MMMs) for gas separation: a review on advanced materials in harsh environmental applications," *Small*, vol. 18, no. 20, p. 2107536, 2022.

[114] A. R. Kamble, C. M. Patel, and Z. Murthy, "A review on the recent advances in mixed matrix membranes for gas separation processes," *Renewable and Sustainable Energy Reviews*, vol. 145, p. 111062, 2021.

[115] S. He, B. Zhu, X. Jiang, G. Han, S. Li, C. H. Lau, Y. Wu, Y. Zhang, and L. Shao, "Symbiosis-inspired de novo synthesis of ultrahigh MOF growth mixed matrix membranes for sustainable carbon capture," *Proceedings of the National Academy of Sciences*, vol. 119, no. 1, p. e2114964119, 2022.

[116] Y. Feng, W. Yan, Z. Kang, X. Zou, W. Fan, Y. Jiang, L. Fan, R. Wang, and D. Sun, "Thermal treatment optimization of porous MOF glass and polymer for improving gas permeability and selectivity of mixed matrix membranes," *Chemical Engineering Journal*, vol. 465, p. 142873, 2023.

[117] K. Zhang, X. Luo, S. Li, X. Tian, Q. Wang, C. Liu, Y. Tang, X. Feng, R. Zhang, S. Yin, *et al.*, "ZIF-8 Gel/PIM-1 mixed matrix membranes for enhanced H_2/CH_4 separations," *Chemical Engineering Journal*, vol. 484, p. 149489, 2024.

[118] A. Kertik, L. H. Wee, M. Pfannmöller, S. Bals, J. A. Martens, and I. F. Vankelecom, "Highly selective gas separation membrane using in situ amorphised metal–organic

frameworks," *Energy & Environmental Science*, vol. 10, no. 11, pp. 2342–2351, 2017.

[119] A. P. Thompson, H. M. Aktulga, R. Berger, D. S. Bolintineanu, W. M. Brown, P. S. Crozier, P. J. in 't Veld, A. Kohlmeyer, S. G. Moore, T. D. Nguyen, R. Shan, M. J. Stevens, J. Tranchida, C. Trott, and S. J. Plimpton, "Lammps - a flexible simulation tool for particle-based materials modeling at the atomic, meso, and continuum scales," *Computer Physics Communications*, vol. 271, p. 108171, 2022.

[120] J. A. Greathouse, "Building lammps data files with car/mdf files and the msi2lmp utility," *Sandia National Laboratories: Albuquerque, NM, USA*, 2010.

[121] Dassault Systèmes Biovia, *Biovia Pipeline Pilot*. Dassault Systèmes, San Diego, Bw, 2024.

[122] CrystalMaker Software Ltd, "CrystalMaker Software Ltd, Oxford, England (www.crystalmaker.com)."

[123] G. Van Rossum, F. L. Drake, *et al.*, *Python Reference Manual*, vol. 111. Centrum voor Wiskunde en Informatica Amsterdam, 1995.

[124] W. Humphrey, A. Dalke, and K. Schulten, "VMD: visual molecular dynamics," *Journal of Molecular Graphics*, vol. 14, no. 1, pp. 33–38, 1996.

[125] A. Stukowski, "Visualization and analysis of atomistic simulation data with OVITO–the Open Visualization Tool," *Modelling and Simulation in Materials Science and Engineering*, vol. 18, no. 1, p. 015012, 2009.

[126] J. Rowlinson*, "The maxwell–boltzmann distribution," *Molecular Physics*, vol. 103, no. 21-23, pp. 2821–2828, 2005.

[127] H. J. W. Müller-Kirsten, *Basics of Statistical Physics*. Hackensack, NJ: World Scientific, second edition ed., 2013. Illustrations; 26 cm.

[128] M. P. Allen and D. J. Tildesley, *Computer Simulation of Liquids*. Oxford University Press, 2017.

[129] D. Frenkel and B. Smit, *Understanding Molecular Simulation*. Elsevier, 1957.

[130] D. Landau and K. Binder, *A guide to Monte Carlo simulations in statistical physics*. Cambridge University Press, 2021.

[131] K. Binder, J. Horbach, W. Kob, W. Paul, and F. Varnik, "Molecular dynamics simulations," *Journal of Physics: Condensed Matter*, vol. 16, no. 5, p. S429, 2004.

[132] G. Battimelli and G. Ciccotti, "Berni alder and the pioneering times of molecular simulation," *The European Physical Journal H*, vol. 43, no. 3, pp. 303–335, 2018.

[133] A. Rahman and P. Vashishta, "Molecular dynamics studies of superionic conductors," in *The Physics of Superionic Conductors and Electrode Materials*, pp. 93–142, Springer, 1983.

[134] D. C. Rapaport, *The art of molecular dynamics simulation*. Cambridge University Press, 2004.

[135] W. C. Swope, H. C. Andersen, P. H. Berens, and K. R. Wilson, "A computer simulation method for the calculation of equilibrium constants for the formation of physical clusters of molecules: Application to small water clusters," *The Journal of Chemical Physics*, vol. 76, no. 1, pp. 637–649, 1982.

[136] L. Verlet, "Computer experiments on classical fluids. I. thermodynamical properties of Lennard-Jones molecules," *Physical Review*, vol. 159, no. 1, p. 98, 1967.

[137] D. Beeman, "Some multistep methods for use in molecular dynamics calculations," *Journal of Computational Physics*, vol. 20, no. 2, pp. 130–139, 1976.

[138] R. W. Hockney and J. W. Eastwood, *Computer simulation using particles*. CRC Press, 2021.

[139] I. Omelyan, I. Mryglod, and F. Reinhard, "Optimized Verlet-like algorithms for molecular dynamics simulations," *Physical Review. E, Statistical, Nonlinear, and Soft Matter Physics*, vol. 65, p. 056706, 06 2002.

[140] J.-P. Hansen and I. R. McDonald, *Theory of simple liquids: with applications to soft matter*. Academic Press, 2013.

[141] M. Doi and S. Edwards, "The theory of polymer dynamics oxford, UK: Oxford Univ," 1986.

[142] H. C. Andersen, "Rattle: A "velocity" version of the shake algorithm for molecular dynamics calculations," *Journal of Computational Physics*, vol. 52, no. 1, pp. 24–34, 1983.

[143] B. A. Wells and A. L. Chaffee, "Ewald summation for molecular simulations," *Journal of Chemical Theory and Computation*, vol. 11, no. 8, pp. 3684–3695, 2015. PMID: 26574452.

[144] G. M. Monsalve-Bravo and S. K. Bhatia, "Modeling permeation through mixed-matrix membranes: A review," *Processes*, vol. 6, no. 9, 2018.

[145] D. Q. Vu, W. J. Koros, and S. J. Miller, "Mixed matrix membranes using carbon molecular sieves: II. Modeling permeation behavior," *Journal of Membrane Science*, vol. 211, no. 2, pp. 335–348, 2003.

[146] H. Vinh-Thang and S. Kaliaguine, "Predictive models for mixed-matrix membrane performance: A review," *Chemical Reviews*, vol. 113, no. 7, pp. 4980–5028, 2013. PMID: 23548158.

[147] A. Idris, Z. Man, A. S. Maulud, and F. Uddin, "Modified Bruggeman models for prediction of CO_2 permeance in polycarbonate/silica nanocomposite membranes," *The Canadian Journal of Chemical Engineering*, vol. 95, no. 12, pp. 2398–2409, 2017.

[148] A. Shariati, M. Omidkhah, and M. Z. Pedram, "New permeation models for nanocomposite polymeric membranes filled with nonporous particles," *Chemical Engineering Research and Design*, vol. 90, no. 4, pp. 563–575, 2012.

[149] Z. Sadeghi, M. Omidkhah, M. E. Masoumi, and R. Abedini, "Modification of existing permeation models of mixed matrix membranes filled with porous particles for gas separation," *The Canadian Journal of Chemical Engineering*, vol. 94, no. 3, pp. 547–555, 2016.

[150] Y. Shen and A. C. Lua, "Theoretical and experimental studies on the gas transport properties of mixed matrix membranes based on polyvinylidene fluoride," *AIChE Journal*, vol. 59, no. 12, pp. 4715–4726, 2013.

[151] A. Kumar, B. J. Walder, A. Kunhi Mohamed, A. Hofstetter, B. Srinivasan, A. J. Rossini, K. Scrivener, L. Emsley, and P. Bowen, "The atomic-level structure of cementitious calcium silicate hydrate," *The Journal of Physical Chemistry C*, vol. 121, no. 32, pp. 17188–17196, 2017.

[152] D. Fan and S. Yang, "Mechanical properties of CSH globules and interfaces by molecular dynamics simulation," *Construction and Building Materials*, vol. 176, pp. 573–582, 2018.

[153] R. T. Cygan, J.-J. Liang, and A. G. Kalinichev, "Molecular models of hydroxide, oxyhydroxide, and clay phases and the development of a general force field," *The Journal of Physical Chemistry B*, vol. 108, no. 4, pp. 1255–1266, 2004.

[154] L. J. Abbott, K. E. Hart, and C. M. Colina, "Polymatic: a generalized simulated polymerization algorithm for amorphous polymers," *Theoretical Chemistry Accounts*, vol. 132, pp. 1–19, 2013.

[155] S. Naskar, D. Fan, A. Ghoufi, and G. Maurin, "Microscopic insight into the shaping of MOFs and its impact on CO_2 capture performance," *Chemical Science*, vol. 14, no. 38, pp. 10435–10445, 2023.

[156] J. L. Asensio, M. Martin-Pastor, and J. Jimenez-Barbero, "The use of CVFF and CFF91 force fields in conformational analysis of carbohydrate molecules. comparison with AMBER molecular mechanics and dynamics calculations for methyl

α-lactoside," *International Journal of Biological Macromolecules*, vol. 17, no. 3-4, pp. 137–148, 1995.

[157] J. A. Greathouse and M. D. Allendorf, "Force field validation for molecular dynamics simulations of IRMOF-1 and other isoreticular zinc carboxylate coordination polymers," *The Journal of Physical Chemistry C*, vol. 112, no. 15, pp. 5795–5802, 2008.

[158] L. Zhou, Y. Liu, C. Zhao, W. Wang, and Y. Yan, "Molecular Insights into the EOR Mechanism of Water, CO_2, and CO_2–WAG Flooding in Heterogeneous Nanochannels: A Molecular Dynamic Simulation," *Langmuir*, vol. 41, no. 9, pp. 6050–6064, 2025.

[159] J. E. Mark, *Polymer data handbook*. Oxford University Press New York, NY, 2009.

[160] A. Habbaba, A. Lange, and J. Plank, "Synthesis and performance of a modified polycarboxylate dispersant for concrete possessing enhanced cement compatibility," *Journal of Applied Polymer Science*, vol. 129, no. 1, pp. 346–353, 2013.

[161] P.-H. Chuang, Y.-H. Tseng, Y. Fang, M. Gui, X. Ma, and J. Luo, "Effect of side chain length on polycarboxylate superplasticizer in aqueous solution: A computational study," *Polymers*, vol. 11, no. 2, p. 346, 2019.

[162] P. Jamshidi Ghaleh, Z. Pinar Haslak, O. Sarbakhshian, H. Öztürk, and I. Erucar, "Pressure-Induced Amorphization of ZIF-8: Deciphering the Role of Atomic Charge Assignments and Adsorbed CH_4 Molecules through Atomistic Insights," *The Journal of Physical Chemistry C*, vol. 129, no. 26, pp. 12068–12082, 2025.

[163] T. Weng and J. Schmidt, "Flexible and transferable ab initio force field for zeolitic imidazolate frameworks: ZIF-FF," *The Journal of Physical Chemistry A*, vol. 123, no. 13, pp. 3000–3012, 2019.

[164] S. Kancharlapalli, A. Gopalan, M. Haranczyk, and R. Q. Snurr, "Fast and accurate machine learning strategy for calculating partial atomic charges in metal–organic frameworks," *Journal of Chemical Theory and Computation*, vol. 17, no. 5, pp. 3052–3064, 2021.

[165] T. Yuan, R. Giro, M. B. Steiner, H. Hsu, and L. Sarkisov, "Emergence of the robeson bound in non-equilibrium molecular dynamics simulations," *ChemRxiv*, 2024.

[166] S. L. Mayo, B. D. Olafson, and W. A. Goddard, "Dreiding: a generic force field for molecular simulations," *Journal of Physical Chemistry*, vol. 94, no. 26, pp. 8897–8909, 1990.

[167] H. A. Lorentz, "Ueber die anwendung des satzes vom virial in der kinetischen theorie der gase," *Annalen der Physik*, vol. 248, no. 1, pp. 127–136, 1881.

[168] D. Berthelot, "Sur le mélange des gaz," *Compt. Rendus*, vol. 126, no. 3, p. 15, 1898.

[169] Z. Peng, Y. Zhou, J. Wang, L. Chen, and C. Miao, "The impediment and promotion effects and mechanisms of lactates on the hydration of supersulfated cements - aiming at a performance enhancement," *Journal of Cleaner Production*, vol. 341, p. 130751, 2022.

[170] Y. Feng, D. Qin, and C. Zhao, "The synergistic strengthening effect of silane coupling agent on the interface between PVA/EPS and cement: experiment and molecular simulation," *Composite Interfaces*, vol. 30, pp. 1–21, 08 2022.

[171] W. Sha, X. Wu, and K. G. Keong, *Electroless copper and nickel-phosphorus plating: processing, characterisation and modelling*. Elsevier, 2011.

[172] M. Kai, L. Zhang, and K. Liew, "Graphene and graphene oxide in calcium silicate hydrates: Chemical reactions, mechanical behavior and interfacial sliding," *Carbon*, vol. 146, pp. 181–193, 2019.

[173] Y. J. Lee, "Concurrent polarization IR analysis to determine the 3D angles and the order parameter for molecular orientation imaging," *Opt. Express*, vol. 26, pp. 24577–24590, Sep 2018.

[174] R. Pal, "Permeation models for mixed matrix membranes," *Journal of Colloid and Interface Science*, vol. 317, no. 1, pp. 191–198, 2008.

[175] A. F. Bushell, M. P. Attfield, C. R. Mason, P. M. Budd, Y. Yampolskii, L. Starannikova, A. Rebrov, F. Bazzarelli, P. Bernardo, J. Carolus Jansen, M. Lanč, K. Friess, V. Shantarovich, V. Gustov, and V. Isaeva, "Gas permeation parameters of mixed matrix membranes based on the polymer of intrinsic microporosity PIM-1 and the zeolitic imidazolate framework ZIF-8," *Journal of Membrane Science*, vol. 427, pp. 48–62, 2013.

[176] P. Li, T. Chung, and D. Paul, "Gas sorption and permeation in pim-1," *Journal of Membrane Science*, vol. 432, pp. 50–57, 2013.

APPENDICES

APPENDIX A. CVFF PARAMETERS FOR CSH/RH COMPOSITE

The CVFF force field parameters for PCE polymer are given as follows:

Table A.1: *Atomic charges and LJ parameters for PCE polymer.*

Atom Name	**Atom Type**	**Charge (e)**	ε **(kcal/mol)**	σ **(Å)**
C	c3	-0.331	0.039	3.876
H	h	$+0.066$	0.039	2.450
C	c	-0.031	0.160	3.474
C	c2	-0.109	0.039	3.875
O	o	-0.261	0.228	2.859
O	oh	-0.411	0.228	2.859
C	c′	$+0.379$	0.148	3.617
C	c1	-0.131	0.039	3.875
O	o′	-0.411	0.228	2.860
H	ho	$+0.319$	0.038	2.450
Na	naoh	$+1.000$	0.115	2.337

The CVFF force field parameters for RH polymer are given as follows:

Table A.2: *Atomic charges and LJ parameters for RH polymer.*

Atom Name	**Atom Type**	**Charge**	ε **(kcal/mol)**	σ **(Å)**
C	c2	-0.1	0.039	3.875
C	c=	-0.2	0.148	3.617
H	h	$+0.1$	0.038	2.450
C	c3	-0.2	0.039	3.875

APPENDIX B. ZIF-FF PARAMETERS FOR ZIF-8/PIM-1 COMPOSITE

The ZIF-FF force field parameters for ZIF-8 are given as follows:

Table B.1: *Atomic charges and LJ parameters for ZIF-8.*

Atom Name	**Atom Type**	**Charge**	ε **(kcal/mol)**	σ **(Å)**
C	C1	$+0.437$	0.086	3.400
C	C2	-0.066	0.086	3.400
C	C3	-0.460	0.086	3.400
H	H2	$+0.114$	0.015	2.510
H	H3	$+0.138$	0.016	2.471
N	N	-0.420	0.170	3.250
Zn	Zn	$+0.707$	0.012	1.960